Turid Danbolt

The Effect of Fe Content on Intergranular Corrosion Behaviour of a 6005 Aluminium Alloy

June 2019

Master's thesis

Master's thesis 2019 Turid Danbolt

NTNU
Norwegian University of
Science and Technology
Faculty of Natural Sciences
Department of Materials Science and Engineering

NTNU
Norwegian University of
Science and Technology

NTNU
Norwegian University of
Science and Technology

NTNU
Norwegian University of
Science and Technology

The Effect of Fe Content on Intergranular Corrosion Behaviour of a 6005 Aluminium Alloy

Turid Danbolt

Materials Science and Engineering
Submission date: June 2019
Supervisor: Otto Lunder
Co-supervisor: Trond Furu

Norwegian University of Science and Technology
Department of Materials Science and Engineering

Preface

This thesis is a continuation of the course *TMT4500 Materials Technology, Specialization Project*, and has been conducted at Department of Materials Engineering, Norwegian University of Science and Technology (NTNU) from January to June 2019. The work is a part of the FICAL project (Fundamentals of Intergranular Corrosion of Aluminium Alloys), a collaboration between NTNU, SINTEF, Hydro, Gränges, Benteler and Steertec.

The author has performed all the experimental work as described in this thesis except for MTEX analysis of EBSD data and TEM sample preparation and analysis, which was conducted by Adrian Lervik (NTNU), and optical emission spectrometry, which was conducted by Trond Furu (Hydro).

Trondheim, June 14, 2019

Turid Danbolt

Acknowledgements

I would like to thank my supervisors, Otto Lunder[1] and Trond Furu[2], for their valuable input and guidance throughout this work. I also want to express my gratitude to Adrian Lervik[3] for his help with EBSD analysis, TEM imaging and valuable insight which has been essential to completing this thesis.

Yingda Yu[4] deserves special recognition for his patience and indispensable help with SEM techniques. I also want to thank Anita Storsve[4] for greatly appreciated help with corrosion experiments.

I am grateful to Berit Vinje Kramer[4], Andreas Hjort[4] and Trygve Schanche[4] for tutoring of laboratory equipment. Thanks to Pål Christian Skaret[4] for help with cutting and Birgitte Karlsen[1] for help with etching. Finally, I would like to thank Helen Langeng[5] for help with extrusion.

[1] SINTEF Industry, Trondheim
[2] Hydro Aluminium, Sunndalsøra
[3] Department of Physics, NTNU, Trondheim
[4] Department of Materials Science and Engineering, NTNU, Trondheim
[5] SINTEF Energy Research, Trondheim

Abstract

The use of aluminium alloys in the automotive industry has been rapidly increasing in the past few years due to incentives to reduce vehicle weight (1, 2). AlMgSi alloys (6000-series) are attractive materials for use in sheets and structural components due to high specific strength, excellent formability and high surface quality. Cu is commonly added to further improve the mechanical properties of AlMgSi alloys. However, Cu additions are proven to introduce corrosion issues due to its ennobling effect (3-5).

Recent studies conducted by Kumari et. al. relates initiation of Intergranular Corrosion (IGC) to the presence of Fe-containing particles on the surface (6). These Fe-containing particles are of the α-Al(Fe, Mn)Si-phase and were found to be effective external cathodes, supplying the necessary cathodic current to sustain IGC. Kumari et. al. proposed that even as these particles corrode rapidly, they continue to act as external cathodes due to redeposition of Cu. In this thesis a 6005-aluminium alloy, henceforth called AA6005, with reduced Fe- and Mn- content was studied to investigate the mechanisms of IGC with minimum α-phase available to serve as external cathodes.

A billet of AA6005 was extruded and subsequently age hardened to naturally aged (T4), artificially underaged (T6x), artificially peak aged (T6) and artificially overaged (T7) condition. Samples of each aging condition, in addition to T6 and T7 temper variants of a 600540-reference alloy containing Fe and Mn, was subjected to accelerated corrosion testing according to EN ISO 11864:2008 method B, which involves immersion in acidified chloride solution.

AA6005 exhibited improved corrosion resistance in all temper conditions compared to the Fe-containing AA6005.40 reference alloy. T4 proved to be the most resistant and displayed limited IGC and etching of the surface even at 120 hours of exposure to acidified chloride solution. Artificial aging lead to transition from uniform IGC at T6x, to localized IGC (T6) and eventually pitting (T7) in the Fe- and Mn-reduced 6005 alloy. The improved corrosion resistance was attributed to reduced availability of external cathodes as well as microstructural alterations and prolonged IGC path.

Sammendrag

Bruken av aluminiumlegeringer i biler øker stadig grunnet ambisjoner om å redusere bilvekten og dermed også drivstofforbruket (1, 2). AlMgSi legeringer, som også betegnes 6000-legeringer, er attraktive materialer til bruk i strukturelle komponenter grunnet høy spesifik styrke, god formbarhet og høy overflatekvalitet. Kobber tilsettes ofte disse legeringene for å forbedre de mekaniske egenskapene. Dette medfører derimot korrosjonsproblemer i ellers korrosjonsbestandige legeringer som følge av kobberets foredlende effekt (3-5).

Nylig pupliserte studier utført av Kumari et. al. tilskriver initiering av Intergranulær Korrosjon (IGC) til jerholdige partikler på overflaten, såkalte α-Al(Fe, Mn)Si partikler (6). Disse partiklene er effektive eksterne katoder og forsyner den nødvendige katodiske strømmen for å framprovosere IGC. Det ble også etablert at selv om disse partiklene korroderer raskt bidrar resterende Cu, et restprodukt av korrosjonen, til vedvarende IGC. I denne oppgaven ble en AA6005-legering, heretter kalt AA6005, med redusert Fe- og Mn-innhold studert for å undersøke fremveksten av IGC med redusert tilgjengelighet til eksterne katoder i form av α-fase.

En bolt AA6005 ble ekstrudert og deretter eldet til naturlig eldet (T4), kunstig undereldet (T6x), kunstig eldet til maksimum hardhet (T6x) og kunstig overeldet (T7) statie. Prøver fra hver eldetilstand, i tillegg til T6 og T7 tilstander av en AA6005.40 referanselegering, ble exponert for akselerert korrosjonstesting. Referanselegeringen ble undersøkt for å gi et sammenlikningsgrunnlag og inneholdt ikke reduserte konsentrasjoner av Fe eller Mn. Akselererte korrosjonstester ble utført ved å nedsenke prøvene i en fortynnet løsning med HCl og NaCl.

AA6005-legeringen viste forbedret korrosjonsmotstand sammenliknet med referanselegeringen ved alle tempertilstander. T4 viste høyest korrosjonsbestandighet, hvor selv 120 timer eksponering for korrosjonsløsning resulterte i begrenset IGC og kun noe etsing av overflaten. Kunstig elding medførte gradvis endring fra uniform IGC ved T6x, til lokal IGC (T6) og til slutt gropkorrosjon (T7). Økt korrosjonsmotstand ble tilegnet redusert tilgang på eksterne katoder, samt mikrostrukturelle endringer som følge av legeringsinnhold, deriblant forlenget IGC gangvei.

Abbreviations

AC	Air Cooled
ADF	Annular Dark Field
BF	Bright Field
BSE	Backscatter Electrons
DF	Dark Field
EBSD	Electron Back-Scatter Diffraction
EDS	Energy-Dispersive Spectroscopy
GB	Grain Boundary
HAADF	High-Angle Annular Dark-Field
HAGB	High Angle Grain Boundary (>15°)
HV1	Hardness Vickers 1 kg load
IGC	Intergranular Corrosion
LAGB	Low Angle Grain Boundary (<15°)
OA	Overaged
PA	Peak aged
PFZ	Precipitation Free zone
SEM	Scanning Electron Microscopy
SSSS	Supersaturated Solid Solution
STEM	Scanning Transmission Electron Microscopy
TEM	Transmission Electron Microscopy
UA	Underaged
WQ	Water Quenched

Table of Contents

1. Introduction

1.1. Background

Aluminium alloys are extensively used in the automotive industry due to suitable mechanical properties, high surface quality and corrosion resistance (1, 7). Wrought and heat treatable aluminium alloys are attractive substitutes for steel due to high specific strength which contributes to reduced vehicle weight (8, 9). AlMgSi alloys (6000-series) are suitable for use in sheets, panels, and structural components due to excellent extrudability and generally high corrosion resistance (7). The high requirements of the automotive industry in terms of mechanical properties can be achieved by alloying with small amounts of Cu or large amounts of Si in excess (5). However, Cu additions and excess Si has been found to introduce corrosion issues, especially susceptibility to intergranular corrosion (IGC) (10).

IGC is localized corrosion on the grain boundaries caused by unfavourable alloying and segregation of solute elements during heat treatment (11). The corrosive attack is difficult to detect with non-destructive methods, and it is therefore important to understand the mechanisms causing it (12). Cooling rates and artificial aging has been found to affect the mode and severity of IGC (13, 14)

In a study conducted by Kumari et. al. IGC initiation in AlMgSi(Cu) alloys was attributed to the presence of iron in the form of α-phase particles on the surface (6, 9). It was proposed that these particles serve as external cathodes and provide the necessary current for self-corrosion and corrosion of the adjacent area. The influence of α-phase as external cathodes and resulting IGC initiation and propagation is investigated in this thesis, as well as relevant microstructural considerations.

1.2. Objective

The primary objective of this thesis is to understand the effect of iron and particularly α-Al(Fe, Mn)Si particles on initiation and propagation of intergranular corrosion (IGC) in extruded AA6005 alloys. As follows, the influence of Fe content on the extruded microstructure is of interest as it

has previously been found to affect propagation of IGC (15, 16). A secondary objective of this work is to determine the propagation of IGC over time.

2. Theoretical Background

2.1. AlMgSi Alloys

The 6000-series, also called AlMgSi alloys, is a subgroup of wrought aluminium alloys with magnesium and silicon as primary alloying elements. Alloys of the 6000-series are commonly used for extruded profiles due to excellent mechanical properties, formability and surface quality (17, 18).

Mg and Si are the main strength contributors due to precipitation of nanoscale Mg_2Si particles, denoted β'', during artificial aging(19, 20). The strength of AlMgSi alloys can by further increased by alloying with Cu. However, Cu additions has been proven to have a detrimental effect on the corrosion behaviour of AlMgSi alloys that are otherwise considered corrosion resistant (3, 4, 10). Other elements such as iron, manganese, chromium, zinc and titanium are often present as impurities or added to the alloy to improve the overall properties. Mn and Cr are added to control the grain size of AlMgSi alloys (19, 21). These elements also prevent recrystallization and somewhat reduce the IGC-susceptibility by binding excess Si in intermetallic phases (5).

Fe is an impurity present in most aluminium alloys and is introduced during melt treatment or originate from recycled aluminium (9, 22). Due to its low solid solubility in aluminium, most Fe is present as intermetallic phases that are formed during casting and homogenization (9, 20, 21).

2.1.1. AA6005

AA6005 is an aluminium alloy belonging to the 6000-series. It is a medium strength, heat treatable alloy with excellent extrudability (23). Its applications include but are not limited to tubing for furniture, ladders and rails. The chemical composition in wt.% of these alloys is presented in Table 2.1.

Table 2.1 Chemical composition range of AA6005 given in wt.% (23).

Al	Mg	Si	Mn	Cr	Cu	Fe	Zn	Ti	Other
Bal.	0.4-0.7	0.5-0.9	0.0-0.5	0.0-0.3	0.0-0.3	0.0-0.35	0.0-0.2	0.0-0.1	0.0-0.15

2.2. Thermomechanical Processing of AlMgSi Extruded Profiles

Extruded aluminium products are produced through a series of thermomechanical processing steps to obtain the desired properties and geometry. The general processing route begin with melt treatment where the aluminium is alloyed, followed by casting, homogenization, extrusion and cutting or forming to the desired final shape. Subsequently, artificial aging is performed to improve the mechanical properties, and finally the profile is anodized or lacquered (7).

2.2.1. Homogenization

Intermetallic compounds such as β-Al_5FeSi and coarse β-Mg_2Si are formed during melt treatment and casting of AlMgSi alloys. These particles have a detrimental effect on the extrudability and further processing (24). Homogenization is heat treatment of the billet prior to metalworking to produce a balanced distribution of elements within the aluminium matrix and remove harmful intermetallic particles (25). When subjected to heat treatment, β-Al_5FeSi particles transform to rounded α-Al(Mn, Fe)Si particles (24). Common industry practice has been to perform homogenization at temperatures 580°C for 2-3 hours (7).

2.2.2. Hot Extrusion

Hot extrusion is an effective metal forming process used to produce long components of complex cross sections. It is extensively used in production of aluminium products due suitable mechanical properties and high formability (7, 26). The process involves pressing a preheated billet through a die with the desired final geometry, followed by immediate water quenching. A conceptual sketch of hot extrusion is included in Figure 2.1. As the metal pass through the die it is heavily deformed due to compressional forces, and the initially large equiaxed grains become elongated and with high concentrations of dislocations. These dislocations act as stored energy within the lattice (27). At elevated temperatures the diffusion rates become adequate for recovery and recrystallization, where the stored energy is relieved through nucleation of new grains on heterogeneities such as dislocations, particles or grain boundaries. The resulting microstructure consist of smaller grains compared to the pre-worked state due to rapid quenching, which contribute to increased hardness by grain refinement (27, 28). Preheating of the billet is a necessary step to remove harmful β-

Mg_2Si particles (7). These particles may cause local melting reactions during extrusion and subsequent tearing due to low eutectic melting point.

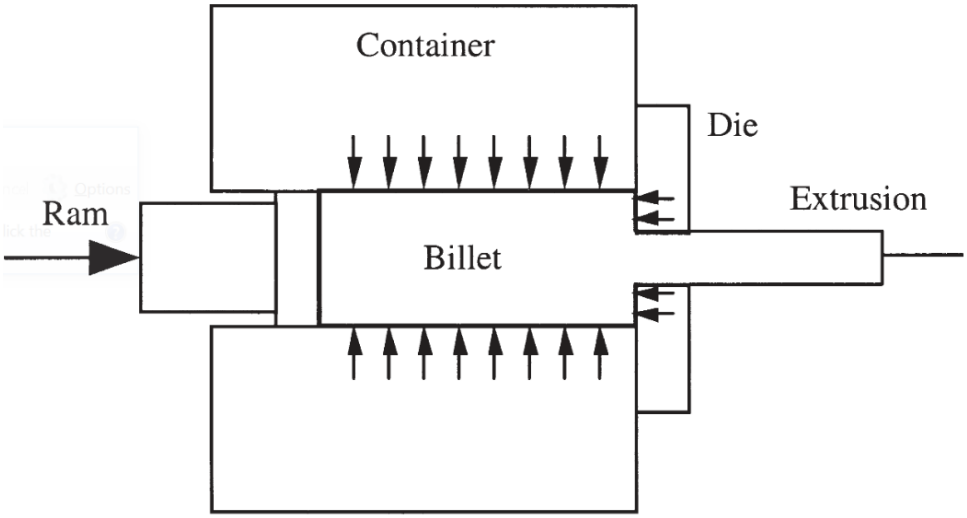

Figure 2.1 Conceptual sketch of extrusion. Reproduced from (26).

2.2.3. Age Hardening

Age hardening or aging is a term used to describe hardening of a metal due to precipitation of hardening phases within the matrix, which progress over time. Natural aging occurs spontaneously at room temperature while the term *artificial aging* is aging at elevated temperatures. The metal is first heated to bring alloying elements into solid solution, called solution heat treatment (SHT), and then rapidly cooled to a state of lower solubility. This results in supersaturated solid solution (SSSS), a state where solute elements are locked within the matrix at above equilibrium concentrations. Over time the solute elements will cluster due to diffusion, and form so called Guinier-Preston (GP) zones which over time precipitates as metastable and eventually stable intermetallic phases. The shape, size and distribution of these precipitates determines the strengthening effect of aging. As these precipitates develop over time the strengthening effect of artificial aging is determined by the aging time (29). Selected temper designations relevant for this thesis is listed in Table 2.2

Table 2.2 Selected temper designations relevant for this thesis. Adapted from (30).

Temper	Definition
T4	Solution heat treated and naturally aged
T6x	Solution heat treated and artificially underaged
T6	Solution heat treated and artificially aged to peak hardness
T7	Solution heat treated and artificially overaged

The precipitation sequence of AlMgSi alloys with a balanced Mg-Si ratio is given in Equation 2.1. where β (Mg_2Si) denotes the equilibrium precipitate. β particles are plate shaped, while the metastable precursors, β'' and β', grow as needles in the matrix (21). Intermetallic phases of other stoichiometries are possible and commonly occur when there is excess Si (31).

$$SSSS \rightarrow atomic\ clusters \rightarrow GP\ zones \rightarrow \beta'' \rightarrow \beta' \rightarrow \beta(Mg_2Si) \qquad (2.1)$$

The hardness evolution of the alloy as it corresponds to the precipitation sequence is illustrated in Figure 2.2. The hardness increases with longer aging time up to the point of overaging where metastable β'' needles are replaced by β' and eventually β particles.

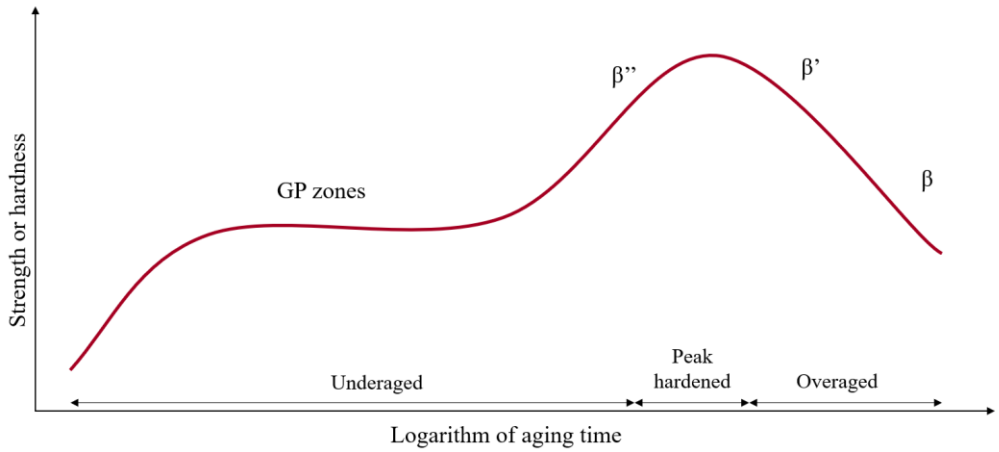

Figure 2.2 Precipitation sequence and corresponding hardness as a function of aging time. Adapted from (27, 31).

Cu additions are associated with increased strength due to higher number density of short needle precipitates. The precipitation sequence of an AlMgSi alloy with Cu additions is presented in Equation 2.2. L and Q' are metastable precursors to the equilibrium phase of the AlMgSi(Cu) alloy

system, which is denoted Q. The Q-phase precipitates outside of the Al matrix and can be found on grain boundaries. L particles are thought to significantly contribute to hardening (31).

$$SSSS \rightarrow atomic\ clusters \rightarrow GP\ zones \rightarrow \beta'', L, QP, QC \rightarrow \beta', Q' \rightarrow Q \qquad (2.2)$$

Precipitate Free Zones

The heat treatment associated with artificial aging also result in migration of alloying elements towards the grain boundaries. Grain boundaries are less ordered than the grain itself due to discontinuous atomic stacking, allowing more room for solute elements (27). The migration of alloying elements from the near vicinity of grain boundaries leaves a solute depleted zone along the grain boundary. As artificial aging is conducted this area will not experience the same strengthening effect due to aging as the grain itself, caused by less alloying elements being available for precipitation. This area is called a Precipitate Free Zone (PFZ) (3).

2.3. IGC Mechanisms

Intergranular corrosion (IGC) is a localized form of corrosion which occurs on grain boundaries and the closely adjacent regions while the grain itself remain unaffected (3, 32). The formation of PFZs in age-hardenable aluminium alloys accompanied with precipitation of intermetallic phases result in local variances in chemical composition in the grain boundary region. These variances give rise to an electrochemical potential difference and thus galvanic coupling between the PFZs and the relatively cathodic bulk or intermetallic phases, resulting in dissolution of the PFZ (3, 9).

2.3.1. Effect of Cu Content

Cu is commonly added to AlMgSi alloys to increase the hardness (8). However, even small copper additions, >0.03 wt.% (21), show detrimental effect on the corrosion resistance of AlMgSi alloys, which is related to the ennobling effect of Cu both as a solute element or bound in intermetallic phases (3, 5). Artificial aging of AlMgSi (Cu) alloys lead to migration of solute Cu and precipitation of Q-phase on grain boundaries. Solute Cu deposits as a continuous film on the grain boundaries as illustrated in Figure 2.3. Both Q phase and Cu-rich GB-film act as cathodes relative to the Al-rich PFZs, which in response will act anodic. A micro galvanic cell is formed between Cu-containing phases and the PFZs, resulting in dissolution of the PFZs when exposed to a corrosive environment (11, 17, 33).

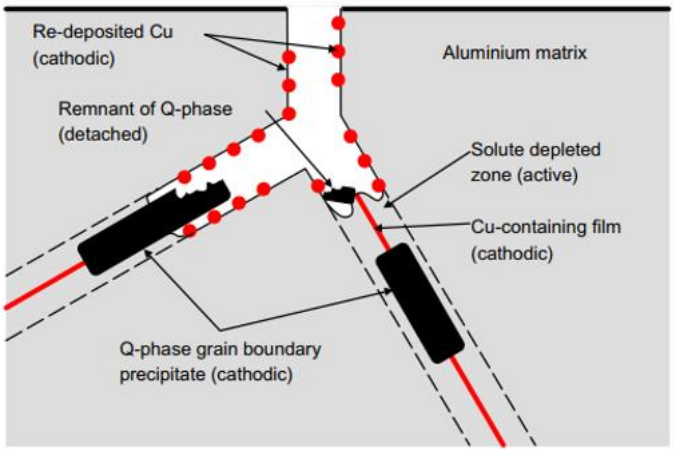

Figure 2.3 Mechanisms of IGC in AlMgSi (Cu) alloys. Reproduced from(13).

Kumari et. al. suggested that the presence of Cu-rich film along GBs with surrounding PFZ is vital to initiation and propagation of IGC in 6000-alloys (9). Q-phase was found to be relatively inert and serve as internal cathodes sustaining IGC if connected to Cu-rich GB film. However, if not connected by Cu-rich GB film, Q-phase particles were proposed to act as physical barriers against IGC propagation (6).

2.3.2. Effect of Artificial Aging

In a study conducted by Svenningsen et. al. it was found that prolonged aging time altered the corrosion mode found in AlMgSi(Cu) alloys, as illustrated in Figure 2.4. Their results showed that exposure to accelerated corrosion tests lead to intergranular corrosion (IGC) at short aging times (underaging), while overaging lead to pitting in air cooled (AC) AlMgSi(Cu) alloys. At the peak aged state, a resistance towards IGC was observed. It was suggested that this was caused by a gradual coarsening of the Cu-film which lead to interruption of the IGC path (13). Increased aging to overaged state promoted coarsening of matrix precipitates, which were thought to serve as initiation cites for pitting (13, 34). However, for water quenched (WQ) samples it was found that natural aging resulted in uniform etching, which transitioned to uniform IGC across the sample surface at underaged state. Aging to peak hardness lead to localized IGC, while overaging lead to coarsening of the IGC path compared to peak aged samples.

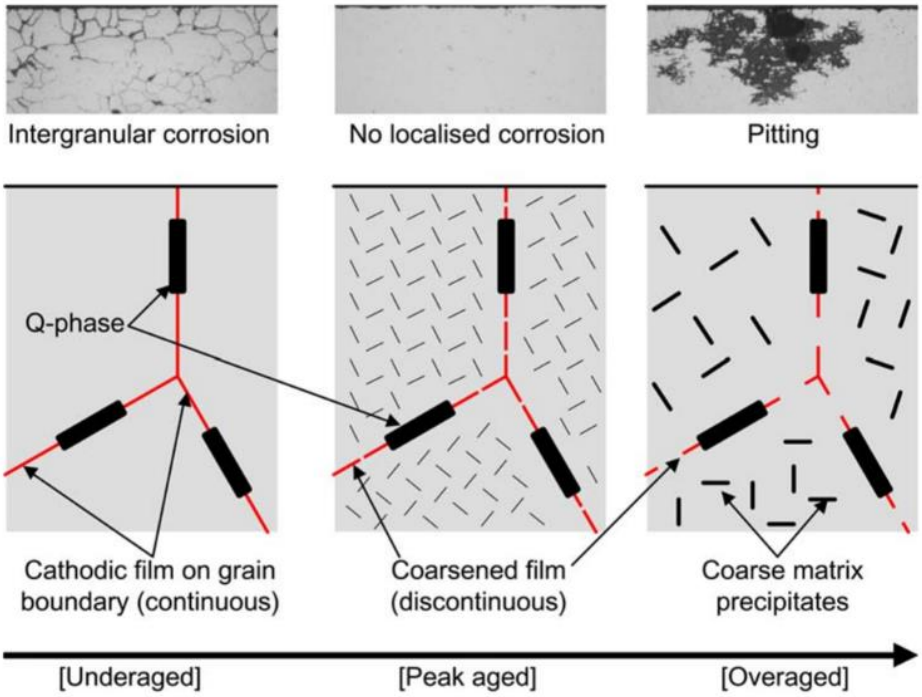

Figure 2.4 Illustrative sketch of the effect of artificial aging on the corrosion mode. Reproduced from (13).

2.3.3. Effect of Microstructure

Several studies have shown that the microstructure influences the resistance to IGC in AlMgSi(Cu) extrusions (12, 35, 36). Both grain size, shape and relative orientation is thought to be relevant for propagation and initiation of IGC and is treated in this section.

Grain Size

Zhang et. al. studied the effect of grain size on sensitization to IGC in a 5000-series aluminium alloy and concluded that smaller grains resulted in a higher resistance towards corrosion (37). This was explained by a lower frequency of grain boundary precipitates as a result of higher total grain boundary area relative to the available solute atoms. However, these results have been disputed and the effects are not yet fully understood (38).

Grain Geometry

Materials subjected to metal forming often exhibit a texturized microstructure. Both experimental and modelling results show a higher IGC growth rate in the longitudinal direction (L) and long transverse direction compared to the short transverse direction (T) (12, 15, 39). The L, T, and S-directions are illustrated in Figure 2.5, where L corresponds to the direction of deformation (12). This was explained by longer IGC path in the S-direction relative to the straighter L and T-directions while the IGC growth rate remain constant. Zhao et. al. simulated IGC propagation in

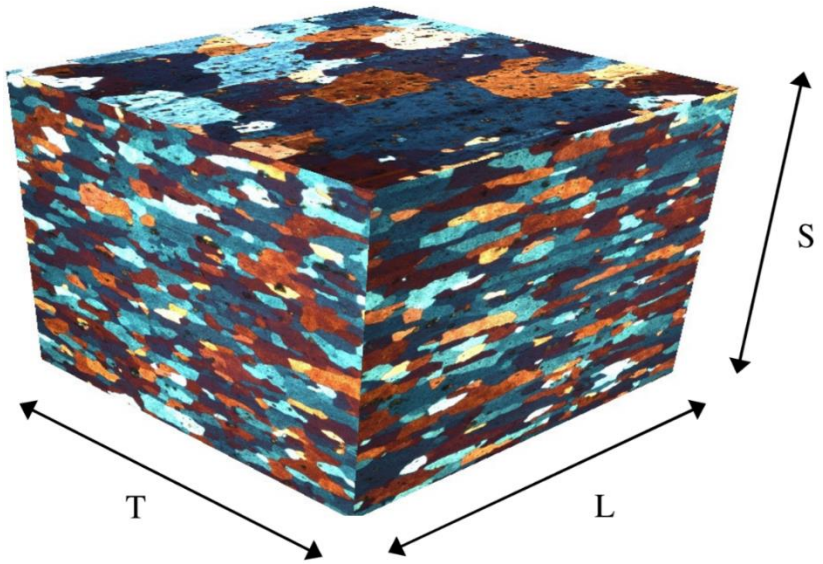

Figure 2.5 Directions in a texturized microstructure. Reproduced from (12).

texturized microstructures using the "brick wall model", and found that it was reasonable to expect elongated grains to provide higher resistance to IGC due to prolonged IGC path compared to equiaxed grains (16, 39).

Grain Misorientation Angle

Grain boundaries are defined as the area of atomic mismatch separating two grains of different crystallographic orientations. Grain boundaries can be classified as either low-angle (LAGB) or high-angle (HAGB) grain boundaries, based on the angle of misalignment between the two neighbouring grains (40). There is an interfacial energy associated with grain boundaries due to less regular bonding of the atoms in this region, which increase with increasing misorientation. Due to higher energy relative to the grain itself, solute elements preferentially segregate to and deposit on grain boundaries (27). In a study conducted by Yan et. al. it was found that there is a correlation between grain boundary angle and IGC susceptibility. They found that LAGBs showed

higher resistance towards corrosion than HAGBs, which was explained by the preferential precipitation of intermetallic particles on HAGBs which serve as cathodes and initiation cites for IGC (35).

2.3.4. Effect of Fe Content on IGC Susceptibility

As previously mentioned, iron is present in commercial aluminium alloys as an impurity from casting or secondary aluminium sources (41). Fe has a solubility of 0.04 wt.% in Al at 655°C, which decreases to less than 0.001 wt.% at room temperature. The low solubility cause most of the iron to be present as intermetallic phases, mainly α- and β-phase (41, 42). Homogenization has been found to increase the density of α-phase over β-phase and solute Fe. Kumari et. al. studied short time IGC in AlMgSi alloys and found that corrosion initiated on α-Al(Fe, Mn)Si particles at the surface (6, 9). Surface α-Al(Fe, Mn)Si particles that were connected to grain boundaries with the necessary conditions to sustain IGC served as effective external cathodes for IGC initiation. Due to rapid corrosion of the particle itself other internal cathodes such as Cu-film and Q-phase were necessary for continued IGC propagation. The results of the study conducted by Kumari et. al. shows that not all α-Al(Fe, Mn)Si particles along GBs serve as initiation sites. A possible explanation was significant variations in composition of the α-phase, attributed to the large stability window in terms of Fe, Mn and Cu content. The lack of IGC initiation on α-phase particles could be related to Cu level in the individual particles or absence of Cu-rich GB film. A residue of Cu was found on the surface where α-phase particles had corroded, and it was suggested that metallic Cu on the surface continued to function as effective external cathodes for IGC initiation.

2.3.5. Effect of Other Common Alloying elements on IGC Susceptibility

Mg and Si

Mg and Si precipitate as hardening phases during heat treatment of AlMgSi alloys. While AlMgSi alloys without Cu are generally considered to be corrosion resistant, excess Si has been related to increased corrosion susceptibility (3, 8). Si in excess corresponds to a Mg to Si ratio lower than 1.73 by weight (43, 44). Elemental Si on grain boundaries have previously been found to act as local cathodes, however, recent studies have indicated that these cathodes are ineffective compared to that of Cu-rich grain boundary film (5).

Mn

AlMgSi alloys are alloyed with Mn to control the grain size (45). Studies have shown that Mn reduces the electrochemical potential difference between the Fe-rich α-phase and the Al matrix due to its ennobling effect in solid solution, and thus reduces the corrosion susceptibility (8, 20). Mn further improves the corrosion resistance by promoting precipitation of AlMnFe-phases at the cost of the more noble Al_3Fe and Al_6Fe phases (9). Due to solubility of Si, Mn-phases has been believed to reduce the susceptibility of IGC by removing excess Si. However, the contribution may be argued to be insignificant due to the inefficiency of excess Si as internal cathodes (5, 21).

Cr

The effect of Cr is similar to that of Mn by binding Fe and removing excess Si, while the effect of the latter may be disputed (9, 21).

2.4. Electron Microscopy Techniques

2.4.1. SEM

Scanning electron microscopy (SEM) is used for high resolution imaging and microstructural characterization (46). A focused electron beam illuminates the sample surface, generating multiple signals that can be detected and provide information about chemical composition, topography and crystallography among others.

EBSD

Electron backscatter diffraction (EBSD) is a SEM tool for crystallographic analysis, and can be used to determine grain orientations, grain boundary misorientation and phase identification (46). The surface investigated must be smooth and free of deformation. EBSD measurements detects electrons scattered due to interactions with atoms in the crystal lattice. Due to regular ordering of atoms in the lattice, constructive or destructive interference of the scattered electron beams will occur. Parallel beams that were scattered by atomic planes will be gathered in a single point on the focal plane by the objective lens, resulting in a diffraction pattern that can further be used for indexing and to determine crystallographic orientations (47). EBSD analysis of a polycrystal will detect the crystallographic orientation of each grain and generate a map of grain orientations.

BSE

Backscattered Electrons (BSE) are high energy electrons that are scattered elastically when interacting with the sample surface. Higher atomic numbers result in higher fractions BSEs, which cause elements of high atomic numbers to appear bright and low atomic number to appear dark.

2.4.2. TEM

Transmission Electron Microscopy (TEM) utilizes electrons generated from a filament and accelerated in an electric field to illuminate the sample (48). This allows for high resolution due to the short wavelength of the electron beam, typically in the range of 2.5 pm. The resolution is limited by aberrations in magnetic lenses, which are used to focus the electron beam. The primary uses of TEM is diffraction and imaging, but it can also be operated as a Scanning Transmission Electron Microscope (STEM) giving different imaging contrast. In addition, the microscope can be equipped with analytical tools for chemical analysis such as Energy-dispersive spectroscopy (EDS).

In TEM mode, if only the direct beam is allowed to pass through the objective aperture a Bright Field (BF) image is produced (47). Particles that scatter the electrons appear dark compared to a brighter background, as the scattered electrons are blocked by the objective. Dark field (DF) images are produced by passing certain scattered electrons through the objective aperture while the direct beam is blocked. Particles that scatter electrons to the region enclosed by the aperture will appear bright, opposite to BF mode.

Some TEM techniques relevant to this thesis is briefly explained below.

STEM

While traditional TEM mode uses a parallel beam of electrons, STEM uses a focused, convergent beam that illuminates a smaller area of the sample, which then is used to scan the desired image area pixel by pixel. Scattered electrons are detected with annular detectors placed at different scattering angles. Commonly used are the Bright Field (BF), Annular Dark Field (ADF) and High-Angle Annular Dark Field (HAADF) detectors (48). The latter can be used to separate atomic columns when observed at high resolution, since the intensity approximately follows a Z^2 relation, where Z is the atomic number (49).

EDS

Energy-dispersive spectroscopy (EDS) detectors are used to separate characteristic x-rays into an energy spectrum, which then is used to determine the presence of specific elements in a material or selected area (46). The characteristic x-rays correspond to element-specific energy differences between two atomic shells and are emitted as exited atoms relaxes to ground state. The exited state is a result of interactions between the electron beam and inner-shell electrons.

3. Experimental

3.1. Materials

A billet of an AA6005 aluminium alloy was supplied by American Elements and studied in this thesis. The alloy was produced for research purposes and contained reduced amounts of Fe and Mn. The billet dimensions were 95 mm in diameter and 210 mm length. An extruded AA6005.40 alloy of similar composition was studied simultaneously for comparison. The 6005.40 alloy was not Fe- and Mn-reduced but had otherwise comparable composition and processing route to the Fe- and Mn-reduced AA6005 alloy. For practical purposes they are called AA6005.40 (reference) and AA6005 from this point. AA6005.40 was supplied by Hydro and has been used in the experiments performed by Kumari et. al. for her PhD thesis (9).

A disc of 10 mm thickness was cut from the AA6005 billet and used in characterization of macrostructure, verification of chemical composition and for measuring hardness and conductivity. The conductivity was measured using a Sigmatest 2.069. Results of billet characterizations are included in Appendix A. Chemical compositions, as measured using optical emission spectroscopy, of both AA6005 and AA6005.40 are presented in Table 3.1 and full analysis results are included in Appendix B and Appendix C. Both alloys contain adequate levels of Cu (>0.1 wt.%) for IGC to be expected and Si in excess (10).

Table 3.1 Chemical composition in wt.% measured using optical emission spectroscopy.

Element (wt.%)	*Al*	*Mg*	*Si*	*Cu*	*Fe*	*Mn*	*Cr*	*Zn*	*Ti*
AA6005	Balance	0.53	0.59	0.13	0.03	0.0005	0.0008	0.0009	0.001
AA6005.40	Balance	0.57	0.64	0.14	0.18	0.14	0.0022	0.0058	0.013

3.2. Thermomechanical Processing

3.2.1. Homogenization

Homogenization of the billet and disc was performed in a Nabertherm N15/65 air circulation furnace preheated to 550°C with 30 minutes hold time. Both the billet and the disc were water quenched after homogenization to avoid formation of coarse β-Mg_2Si particles (24).

3.2.2. Hot Extrusion

Hot extrusion was performed in a vertical laboratory press at SINTEF. The billet was first preheated to 480°C using induction. The heated billet was pressed through a die of 3x65mm dimensions to produce a profile of rectangular cross section. Extrusion parameters are included in Appendix D. The extruded sheet entered a water bath after exiting the die for water quenching (WQ) and was subsequently cut into eight sections and stored in a freezer to avoid undesirable effects of natural aging. Due to the distance between the die and the water bath, the end section of the profile experienced air cooling (AC) after extrusion. Steady state was assumed in the middle section of the profile.

3.2.3. Artificial Aging

Artificial aging of AA6005 was performed in a Nabertherm N15/65 air circulation furnace at 185°C. The holding time was varied to produce underaged (UA), peak aged (PA) and overaged state (OA), further denoted as T6x, T6 and T7 respectively. Table 3.2 provides an overview of the aging parameters for each aging state. The material was inserted into the preheated furnace and air cooled to room temperature after the specified aging time. Prior to heat treatment the material was exposed to room temperature for approximately 30 minutes. A naturally aged variant, denoted T4, was included in further experiments for comparison. AA6005.40 was supplied in T6 state and a T7 version was obtained by additional aging for 19 hours, resulting in a total artificial aging time of 24 hours. The T6 temper of AA6005.40 had been exposed to room temperature for approximately 2 hours prior to artificial aging (9).

Table 3.2 Artificial aging temperature and holding time to achieve designated tempers.

Temper designation	Temperature (°C)	Hold time (hours)
T4	RT	n/a
T6x	185	1
T6	185	5
T7	185	24

3.3. Microstructure Characterization

The microstructure of AA6005 and AA6005.40 was examined using optical microscopy.

3.3.1. Sample Preparation for Optical Microscopy

Prior to microstructural characterization several sample preparation steps were performed. Pieces of the material were cut into samples of approximately 2.5x1.5 cm using a Struers Labotom-5, before mounting the samples in epoxy made from a mixture of 25 parts Epofix resin and 3 parts Epofix hardener. The epoxy cured for more than 12 hours before the samples were removed from the cast. To obtain a planar sample surface for microstructure examination, the samples were first grinded using SiC abrasive paper in the order P320, P500, P800 and P1200, followed by polishing with subsequently 9µm, 3µm, 1µm and finally 0.25 µm diamond suspension using Tegramin-30. Once the final polishing step was finished the polished surface of each sample was anodized by lowering into a *5%* HBF_4 solution and applying 20V for 90 seconds.

3.3.2. Optical Microscopy Imaging

A Leica MEF4M optical microscope was used for characterization of the microstructure of the two alloys. The images were captured os the longitudinal cross section at the top edge to observe the surface microstructure, as illustrated in Figure 3.1. Anodized samples were studied using crossed polarisers and a subparallel λ-plate to accentuate the microstructure.

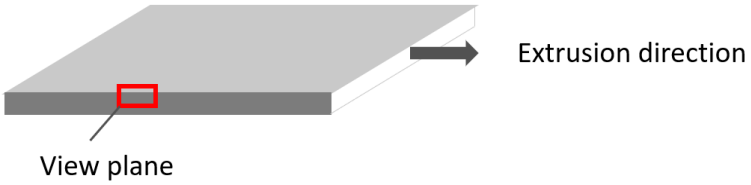

Figure 3.1 Schematic demonstration of the view plane as captured in optical microscope.

The grain size was determined according to ASTM-E112 (50). Three equally long lines were drawn across the optical microscopy image; one vertical, one horizontal and one diagonal. The number of grains crossed for each line was counted and average grain size calculated by first adjusting for the length of the lines relative to the scale bar and then dividing by the average number of grains crossed. An illustration if the method is depicted in Figure 3.2.

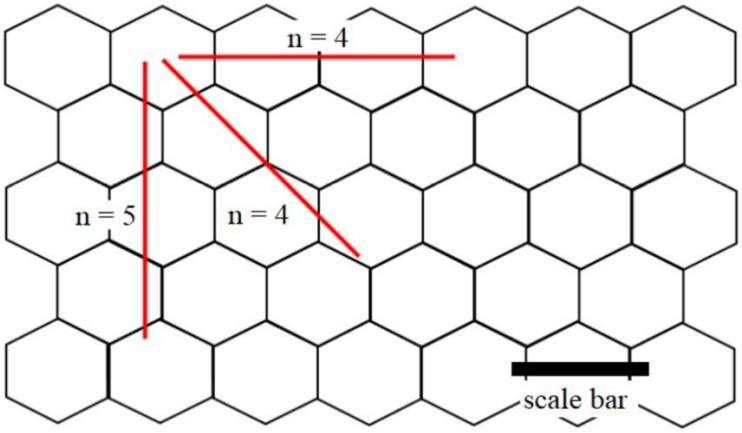

Figure 3.2 Illustration of method used to determine the grain sizes. The honeycomb structure illustrates the microstructure, while the red lines represent the lines drawn on the optical micrograph and n is the number of grains crossed by each line. Reproduced from (51).

3.4. SEM and TEM examination

Scanning electron microscopy (SEM) and transmission electron microscopy (TEM) was used to study the microstructure, grain boundaries and precipitation. TEM analysis and sample preparation was performed by Adrian Lervik.

3.4.1. Scanning Electron Microscopy

Sample preparation

Samples investigated in SEM were first grinded and polished as described in section 3.3.1, before a final vibropolishing step using VibroMet 2 for 4 hours. The epoxy was separated from the metal to avoid surface charging in the electron microscope. This was achieved by immersing the samples in liquid nitrogen for a few minutes before detaching the epoxy.

Electron Backscatter Diffraction

Electron backscatter diffraction (EBSD) was performed on the cross section of selected tempers for investigation of grain boundary characteristics. The EBSD images were obtained using a Hitachi SU-6600 FESEM with 24.5 mm working distance (WD), 20 kV, 50X magnification and a 70°-tilt angle to position the sample normal to the EBSD detector. Nordif3 was used for indexing the diffraction patterns, OIM was used to develop EBSD maps, and MTEX was used for image processing.

3.4.2. Transmission Electron Microscopy

Sample preparation

Transmission Electron Microscopy (TEM) specimens were prepared by mechanical grinding down to ~100 µm foil thickness using SiC abrasive paper. From the foil, disc with 3 mm diameter were punched out and subsequently electropolished using a Struers TenuPol-5 device. An electrolyte of 1/3 HNO_3 and 2/3 CH_3OH was used and kept at temperatures between -30 and -20 °C with an applied potential of 20 V.

Microscopes and techniques

All studied tempers were investigated in an JEOL JEM-2100F operated at 200 kV and equipped with an Oxford X-max 80 silicon drift detector for the Energy Dispersive X-ray Spectroscopy (EDS) analysis. The microscope was operated both in conventional TEM mode and Scanning Transmission Electron Microscopy (STEM) mode. All EDS was performed in STEM mode using a 1.0 nm probe size. Both Bright Field (BF) and High-Angle Annular Dark-Field (HAADF) images were obtained in STEM. BF-STEM gives scattering contrast like that in conventional BF-TEM (strong scattering regions appear dark), while HAADF gives intensity according to the scattering element (48).

The T7 temper were additionally studied in a Cs-corrected JEOL ARM200CF operated at 200 kV, with 0.08 nm probe size, convergence semi-angle of 28 mrad and 35 mrad inner collector angle. This instrument enables high resolution imaging of precipitate crystal structure using the HAADF detector, were the intensity in the image scales approximately according to Z^2 (49).

3.5. Hardness Measurement

Vickers hardness of the materials were measured using a Zwick Roell measuring instrument. Samples of each temper were indented on the top surface of the sheet as illustrated in Figure 3.3. Eight indentations were conducted on each sample with a load of 1 kg and dwelling time of 10 seconds. The indents were made 1 mm apart to avoid interference. The average of the eight measurements was further used as descriptive of the material hardness. Vickers hardness is calculated according to Equation 3.1, where F is the applied load in kg and D^2 is the indentation area in mm^2 (52).

$$HV = 1.854\frac{F}{D^2} \tag{3.1}$$

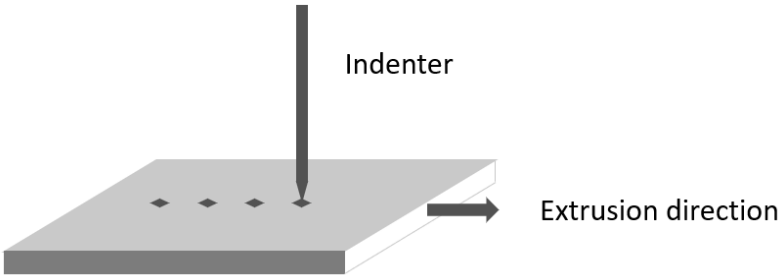

Figure 3.3 Indentation of sample material.

3.6. Accelerated IGC Tests

Corrosion tests were executed according to the EN ISO 11846:2008 standard method B, to investigate the susceptibility to intergranular corrosion of the extruded material. The standard is developed for use on heat treatable and uncoated aluminium alloys. The exposure time was varied from 1 to 120 hours, using three parallels of each alloy and temper combination.

3.6.1. Sample Preparation

Samples with dimensions 20x30 mm were cut from the extruded and artificially aged profiles using Struers Labotom-5, where the longer side corresponded to the extrusion direction. The newly cut edges were then grinded with P500 SiC abrasive paper to remove debris from cutting.

Several cleaning steps were performed in preparation for corrosion tests, as specified in the standard. The samples were first degreased with acetone and then immersed in a 5-10% sodium hydroxide solution (NaOH) heated to 50-60°C for 2.5 minutes. Thereafter the samples were rinsed in running distilled water before they were further submerged in a solution of 68% concentrated nitric acid for 2 minutes. Remaining products from cleaning and desmutting steps were rinsed off in running distilled water.

3.6.2. IGC tests

The corrosion tests were executed by immersing the samples in a solution of 10ml/l hydrochloric acid (HCl) and 30 g/l sodium chloride (NaCl). The solution was prepared by mixing 15 ml of 37% HCl, 45 g NaCl and distilled water in a volumetric flask. The hydrochloric acid, solid NaCl and most of the distilled water were added first and thoroughly mixed, before distilled water was added until 1.5 L solution was obtained. A ratio of 5 ml solution per cm^2 sample area was used in the experiments to satisfy the requirements in the standard.

The solution was poured into a wide beaker and the samples were placed upright against the beaker wall with the shorter edge at the bottom to maximize the area in contact with the solution. The duration of exposure to the corrosive solution was varied to determine the initiation and the propagation of IGC or pitting over time. After the samples were removed from the beaker, they were scrubbed with a non-metallic brush and rinsed in distilled water, before further cleaning in concentrated nitric acid for a few minutes to remove any remaining corrosion products. The samples were weighed with a 0.1 mg precision scale directly before immersing in the corrosive solution and again after the final cleaning step to record the corrosion rate.

The corroded samples were examined in optical microscope to study the severity and nature of the corrosive attack. Samples of all temper variants were grinded and polished as described in section 3.3.1 and the cross section parallel to the rolling direction was examined in a Zeiss Axio optical microscope.

4. Results

4.1. Optical Microscopy

Fe-reduced samples show full recrystallization after hot extrusion and equiaxed grains, as can be seen in Figure 4.1. The grains are somewhat smaller close to the sample surface compared to the centre. The grain size was measured to 100.9 μm for the T6 temper of Fe-reduced. Aging does not affect the microstructure and it can therefore be assumed that this is equal for all temper conditions.

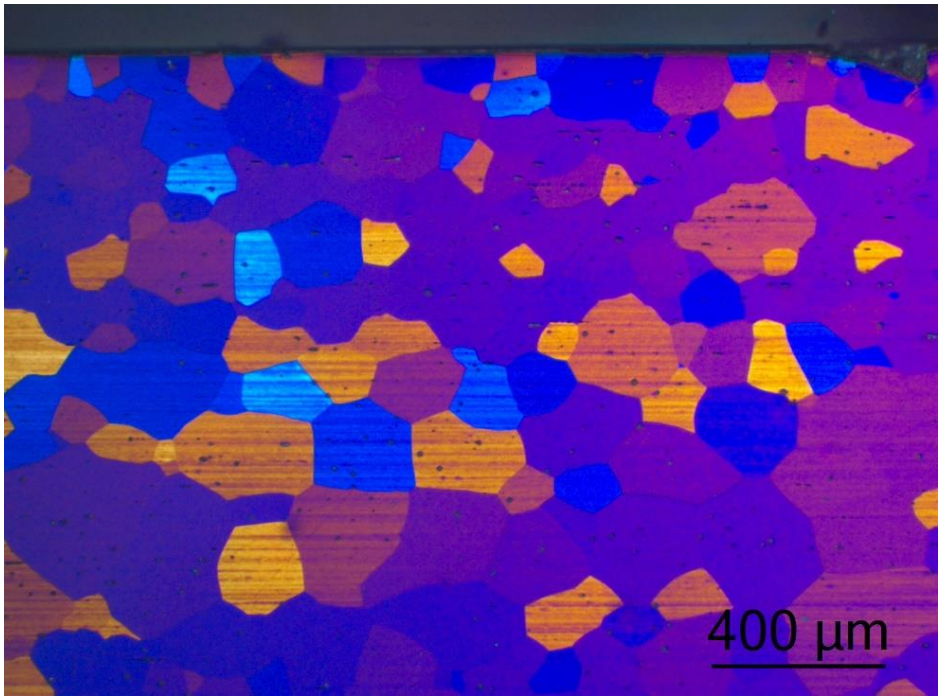

Figure 4.1 Optical micrograph of AA6005. The micrograph is captured of the T6 temper, but similar microstructure is found in all tempers.

AA6005.40 has varying grain size through the cross section which can be treated as four layers; layer 1 is the surface layer with relatively small grains, layer 2 consist of larger grains that appear elongated in the direction perpendicular to the extrusion direction, layer 3 have large grains elongated in the direction of extrusion, and finally layer 4 is the bulk.

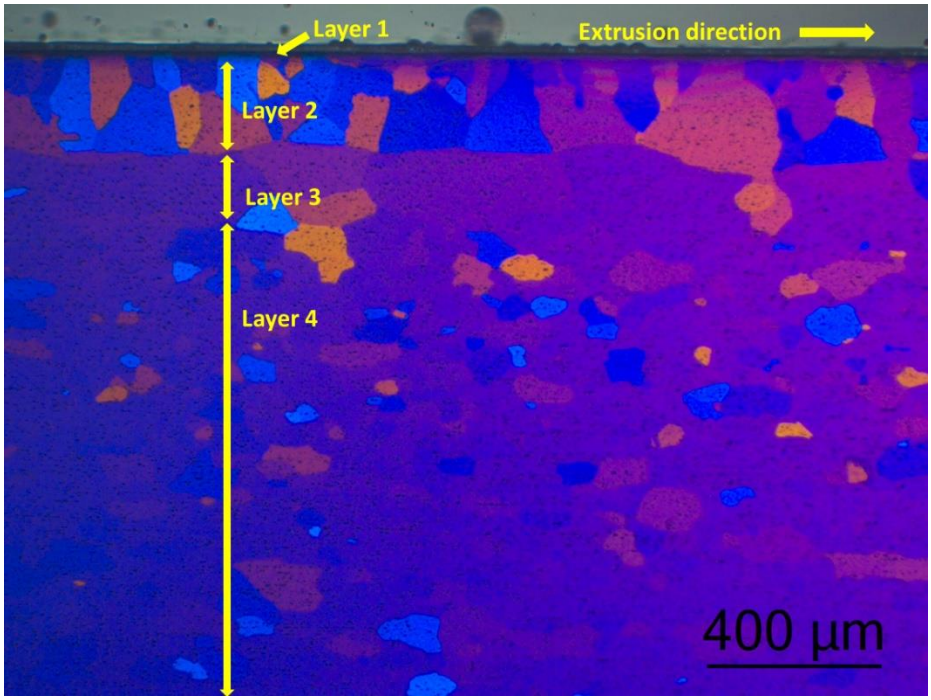

Figure 4.2 Optical micrograph of AA6005.40. The micrograph is captured of the T6 temper, but similar microstructure is found in all tempers.

4.2. EBSD

Figure 4.3 shows the cross-sectional EBSD map of AA6005 and AA6005.40 respectively. The images are captured near the surface to study the surface region as well as the bulk. EBSD maps developed with OIM have been processed with MTEX to remove noise and smooth the grains. It can be observed that AA6005 consist of mostly equiaxed and large grains in the bulk compared to AA6005.40. AA6005 does not have similar microstructural layering as AA6005.40.

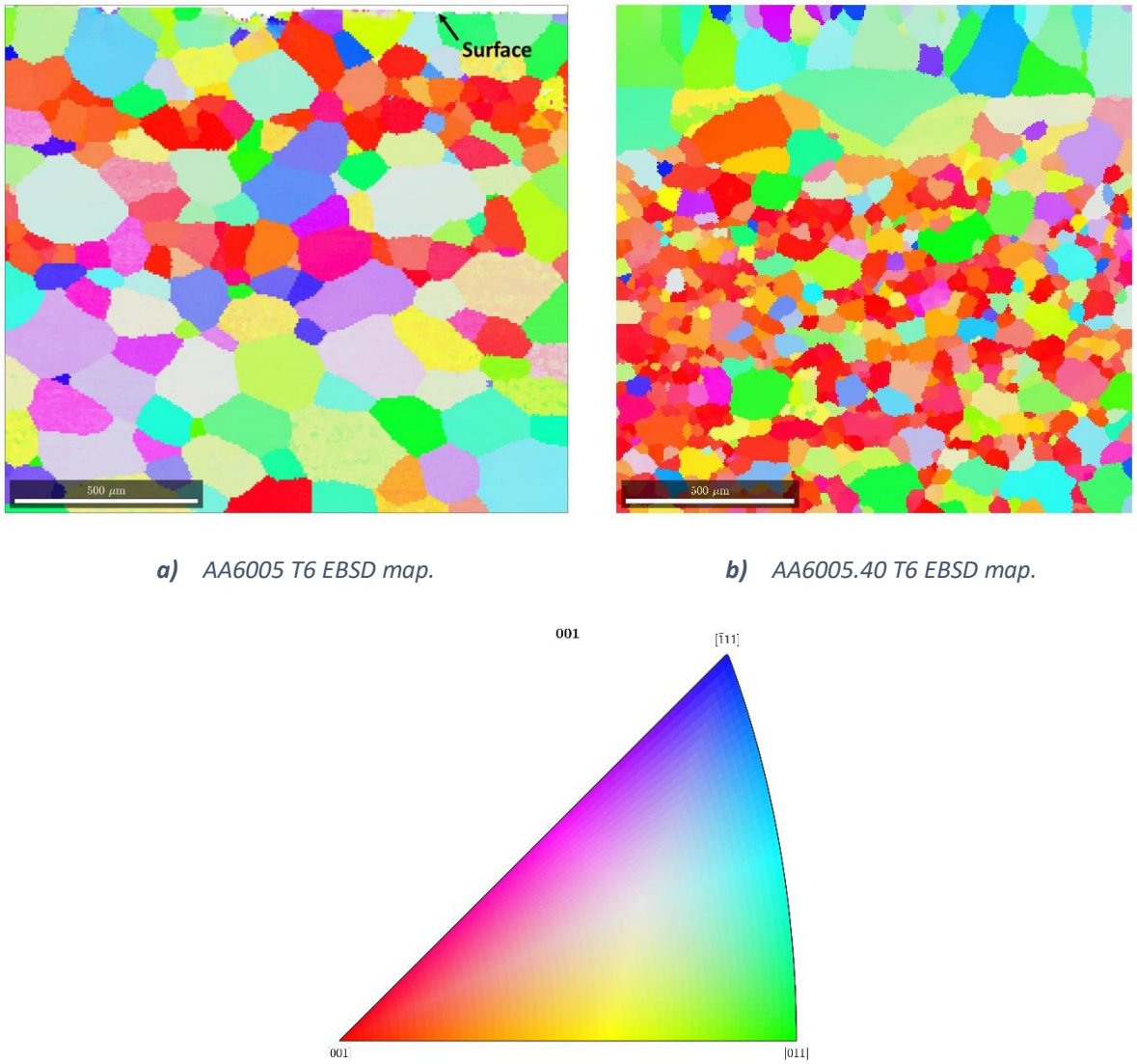

a) *AA6005 T6 EBSD map.*

b) *AA6005.40 T6 EBSD map.*

c) *Grain orientation index.*

Figure 4.3 EBSD maps of the two alloys with grain orientation represented through the inverse pole figure colouring scheme in figure c..

EBSD maps were used to determine the grain boundary misorientation. Figure 4.4 shows cross-sectional EBSD maps of respectively AA6005 and AA6005.40 with highlighted grain boundaries. Each grain boundary is assigned a shade, where brighter shades indicates low angle grain boundaries (LAGBs) and darker shades indicate high angle grain boundaries (HAGBs). The bulk region of AA6005.40 consist of many small grains with low misorientation angles, while the bulk region in AA6005 is dominated by larger equiaxed grains with higher misorientation angles.

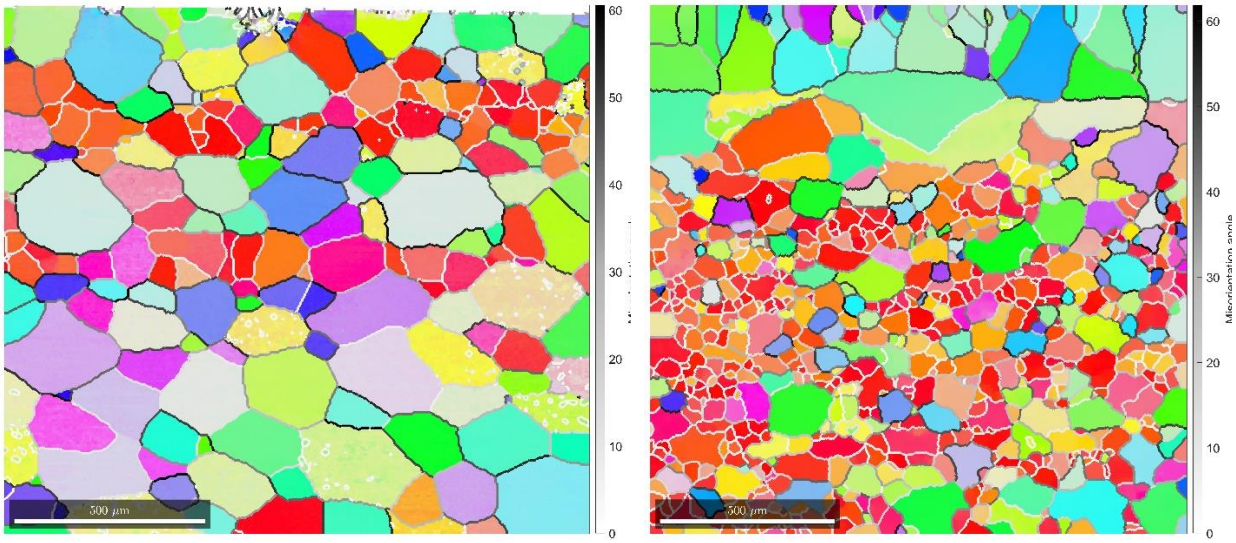

a) *AA6005 T6.* ***b)*** *AA6005.40 T6*

Figure 4.4 Mapped misorientation angle. Shading indicates misorientation angle according to gradient bar on the right.

The distribution of misorientation angles in the surface region of AA6005 and AA6005.40 is represented in Figure 4.5, plotted with frequency on the y-axis and misorientation angle on the x-axis. The lower misorientation limit is set to 5° to remove errors from signal disturbance. Some grain boundaries with low misorientation angle may be excluded from the plot due to the lower limit. The distribution is normalized to make up for smaller grains and thus a higher total number of grains in the AA6005.40. The histograms compare the distribution of misorientation angle of a surface region and bulk region. Both alloys show an increase in HAGBs near the surface compared to the bulk region, while the trend is more prominent in AA6005.40. The bulk in both alloys show a concentration peak between 5° and ~15° misorientation for the bulk region.

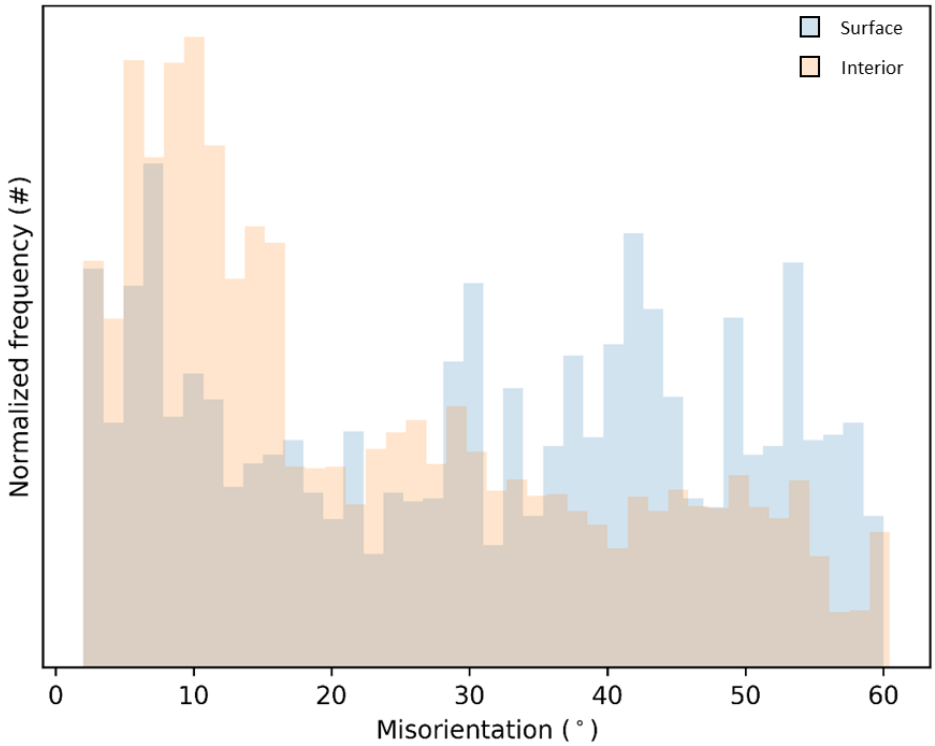

a) *AA6005 T6.*

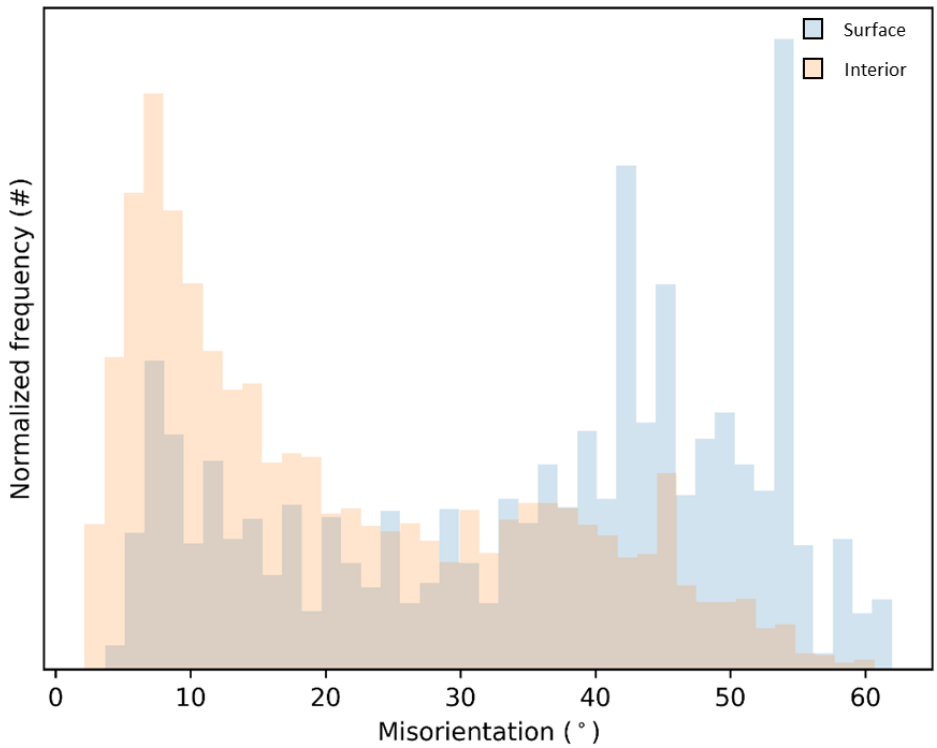

b) *AA6005.40 T6.*

Figure 4.5 Normalized frequency of GB misorientation angle of surface region and bulk (interior).

4.3. TEM

Samples of AA6005 were studied in transmission electron microscope (TEM) to investigate the occurrence of precipitates in bulk and on grain boundaries as well as the presence of Cu-rich GB-film. T6x, T6 and T7 tempers were studied.

T6x

BF-STEM images and EDS analysis of AA6005 T6x are included in Figure 4.6 and Figure 4.7. EDS analysis of a GB, as seen in Figure 4.6, show segregation of Cu and formation of continuous Cu-rich GB film. The Cu-rich film is interrupted by a large GB precipitate, which likely is Q-phase as accumulation of Mg, Si and Cu can be seen in the EDS analysis. Figure 4.7 shows another GB with Q-phase precipitates, but where no Cu-film is observed. Instead several Q-phase precipitates are found on the GB.

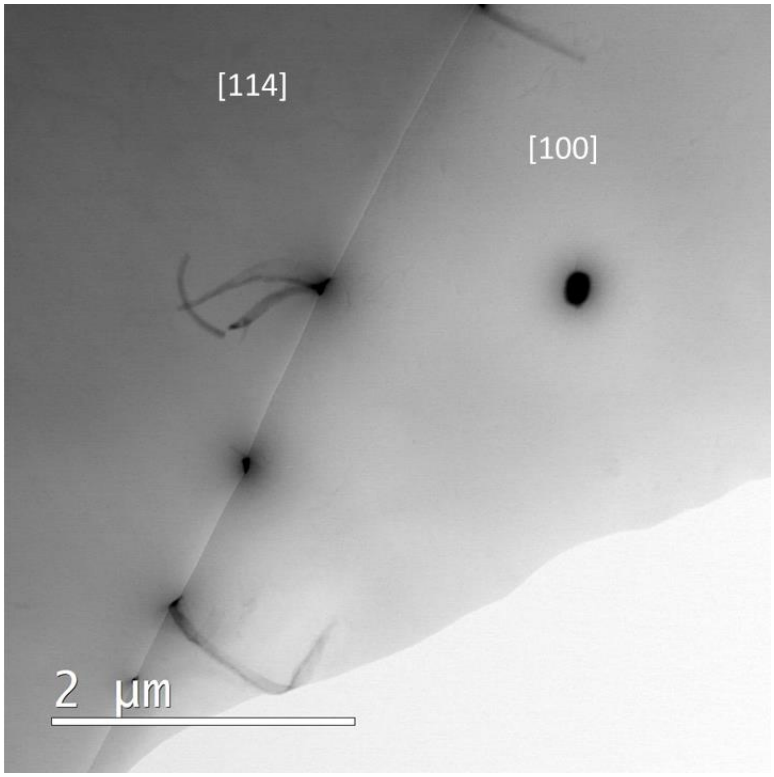

a) *BF image of GB with large Q-phase precipitates between two grains oriented close to [114] and [100] axis, respectively, with large Q-phase precipitates present at the GB.*

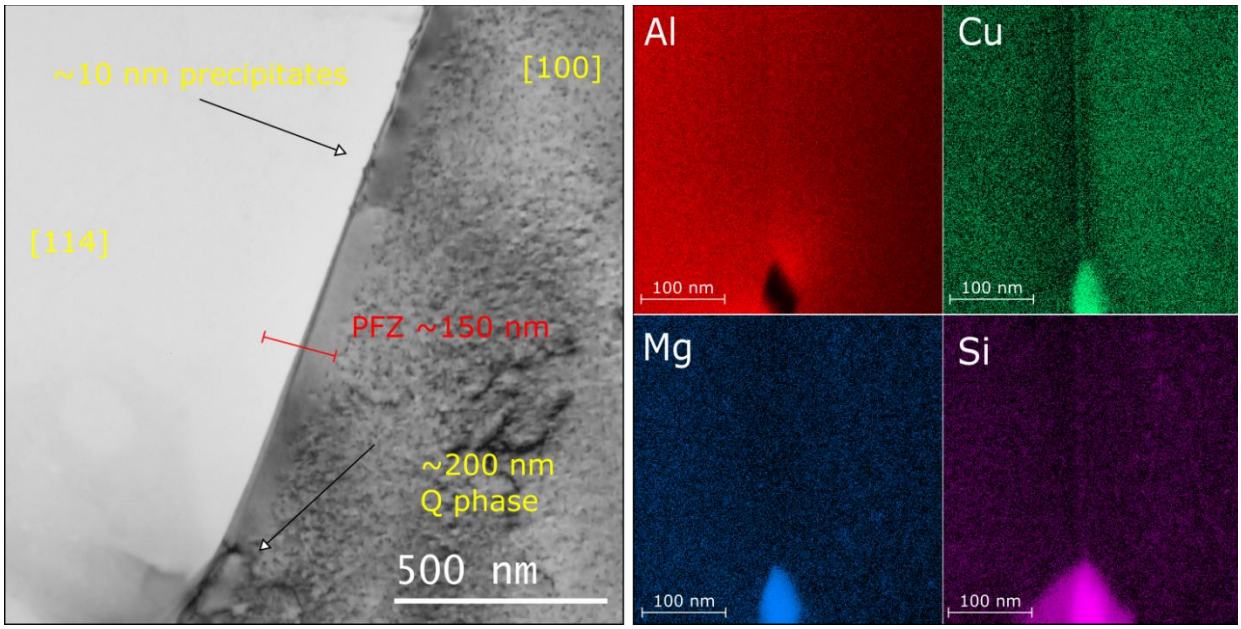

b) *BF-STEM and EDS analysis of the GB.*

Figure 4.6 AA6005 T6x GB with large Q-phase precipitates. ***a)*** *TEM image of GB. The scale bar is 2 µm.* ***b)*** *Magnified BF-STEM at the GB near a precipitate. EDS analysis reveal segregation of Cu to the GB.*

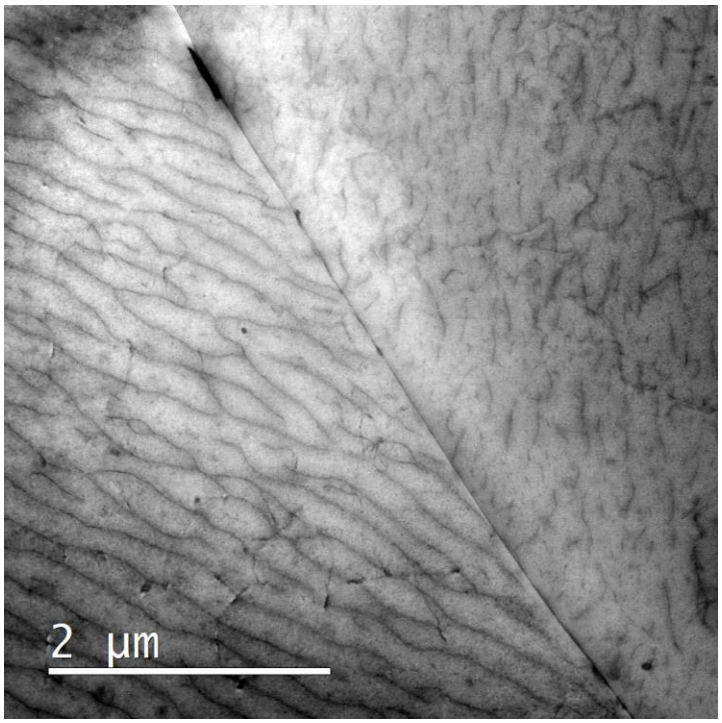

a) *BF image of GB with Q-phase precipitates.*

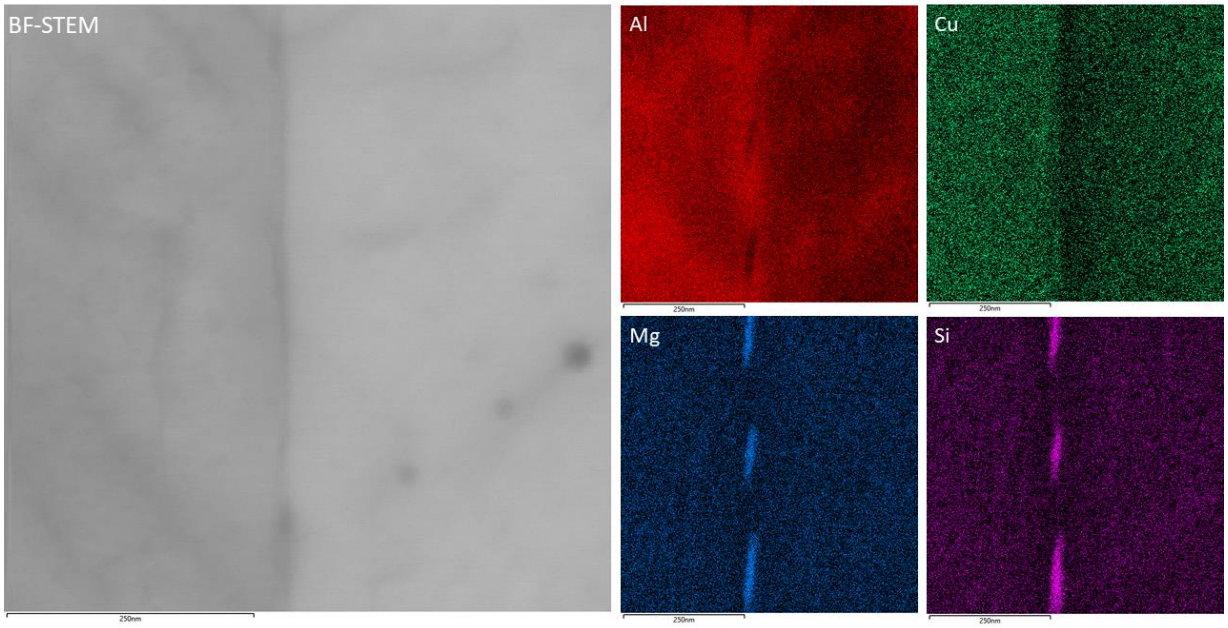

b) *BF-STEM and EDS analysis of the GB.*

Figure 4.7 AA6005 T6x GB with Q-phase precipitates. Dislocations observed in the grain. ***a)*** *BF image of GB. The scale bar is 2 µm.* ***b)*** *Magnified BF-STEM at the GB near a precipitate. EDS analysis show no indications of Cu segregation. The scale bar is 250 nm.*

BF-TEM images of T6x show precipitations on dislocations in the bulk in addition to formation of hardening precipitates, as seen in Figure 4.8. Images are captured along the [100]-direction.

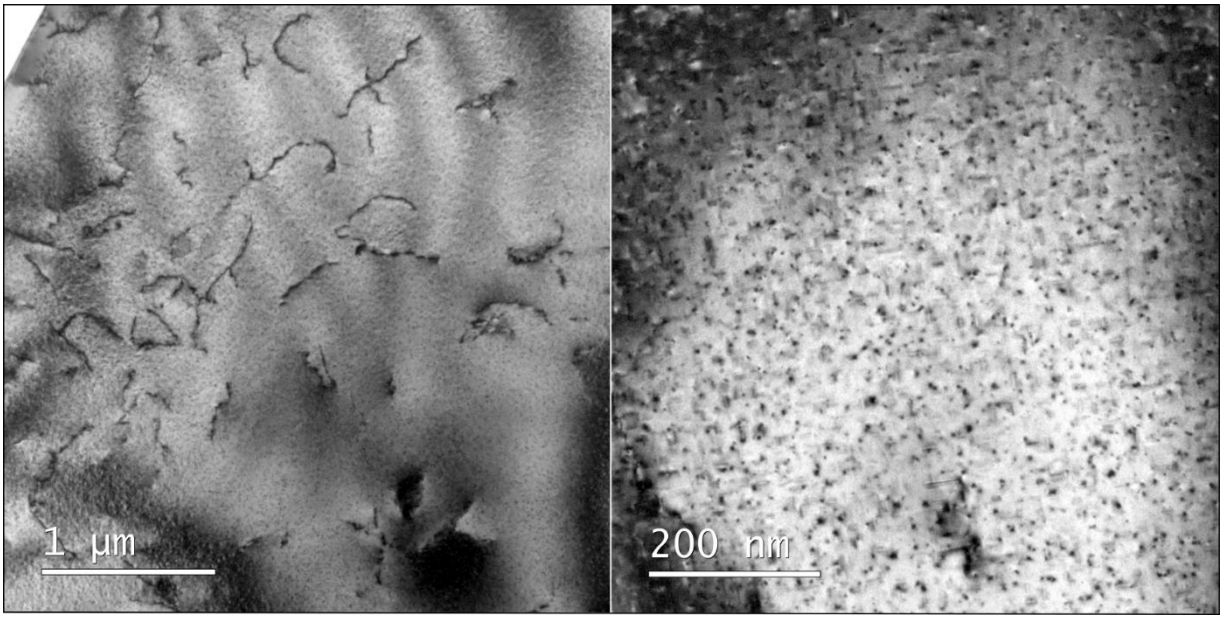

a) *Dislocations with precipitates.* ***b)*** *Hardening precipitates in T6x bulk.*

Figure 4.8 BF-TEM images of AA6005 T6x bulk.

T6

Figure 4.9 shows BF-STEM images of AA6005 T6 at a grain boundary with rotation. Precipitates have formed on the GB prior to rotation, while none are found after. This suggest selective precipitation on certain GB planes as the misorientation is the same along the entire GB. EDS mapping of GB regions indicate that the GB precipitates contains Mg, Si and some Cu which suggests Q-phase precipitates. Faint observations of Cu-rich GB-film can be made from EDS maps of the precipitate-free GB.

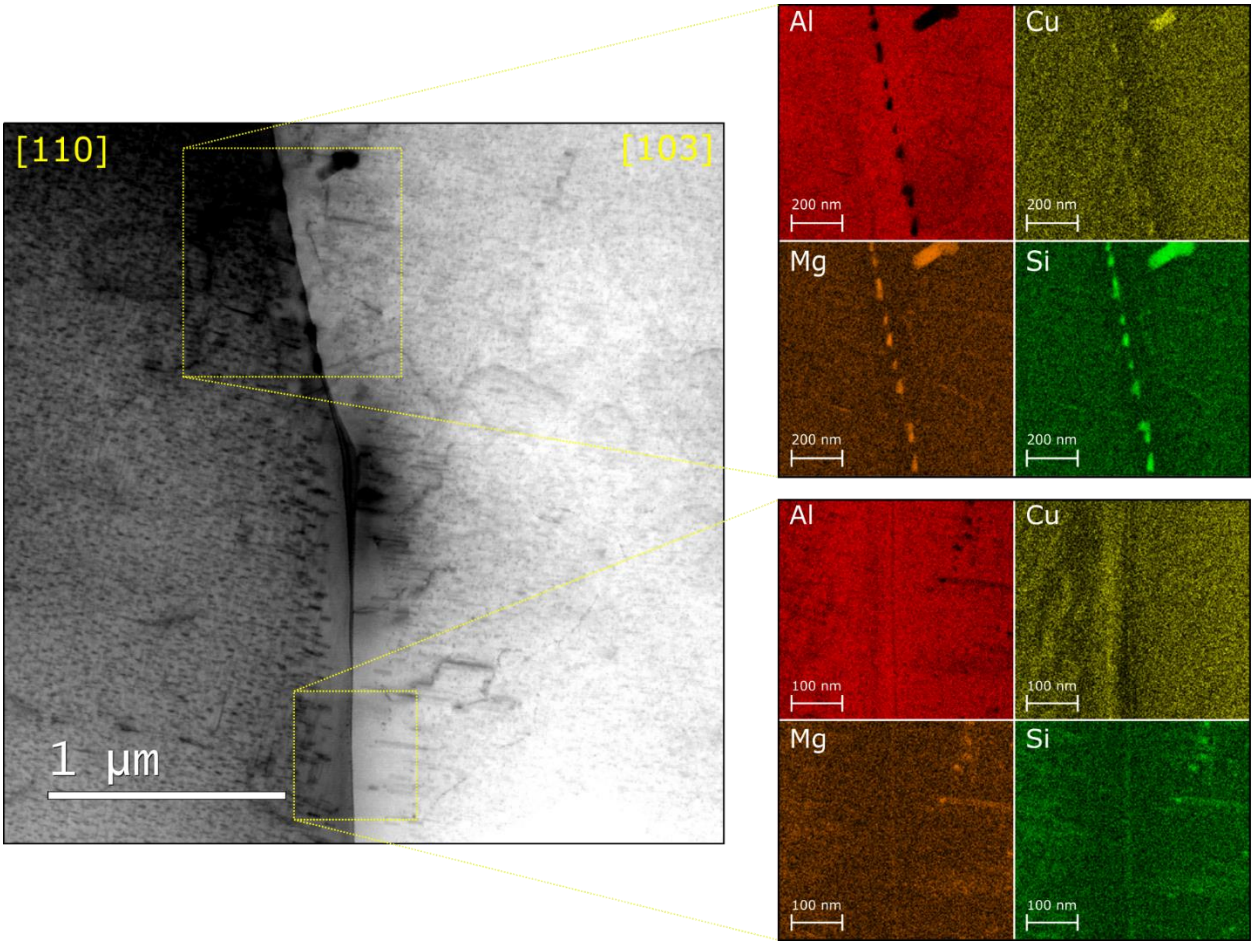

Figure 4.9 BF-STEM and EDS analysis of a grain boundary in AA6005 T6. EDS analysis of regions highlighted by yellow squares are included on the right.

BF-TEM images of T6 show large Mg_2Si particles heterogeneously nucleated in the bulk, as seen in Figure 4.10a. Figure 4.10b shows nano-sized hardening precipitates in the bulk.

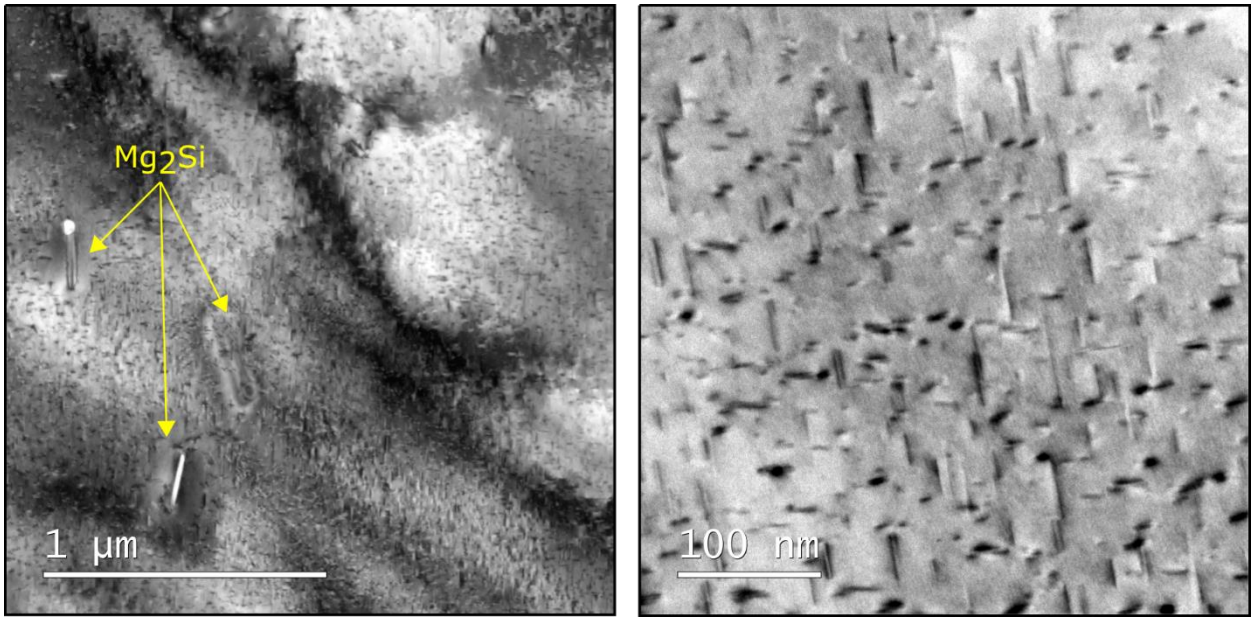

a) *Mg_2Si particles observed in T6 bulk.* ***b)*** *Hardening precipitates observed in T6 bulk.*

Figure 4.10 BF-TEM and BF-STEM images of T6 bulk acquired along the [110] aluminium direction.

T7

Figure 4.11 show precipitation of Q-phase on GBs in AA6005 T7 temper. EDS scans, as depicted in Figure 4.12, are captured from the precipitate-free region of the GB in Figure 4.11, where a continuous Cu-rich GB film is more likely. Mapping of Cu concentrations show no indications of such Cu segregation or continuous GB film. Metastable Q' precipitates was also found within the bulk as illustrated in Figure 4.13. These precipitates incorporate large amounts of Cu, which may explain the absence of Cu-film.

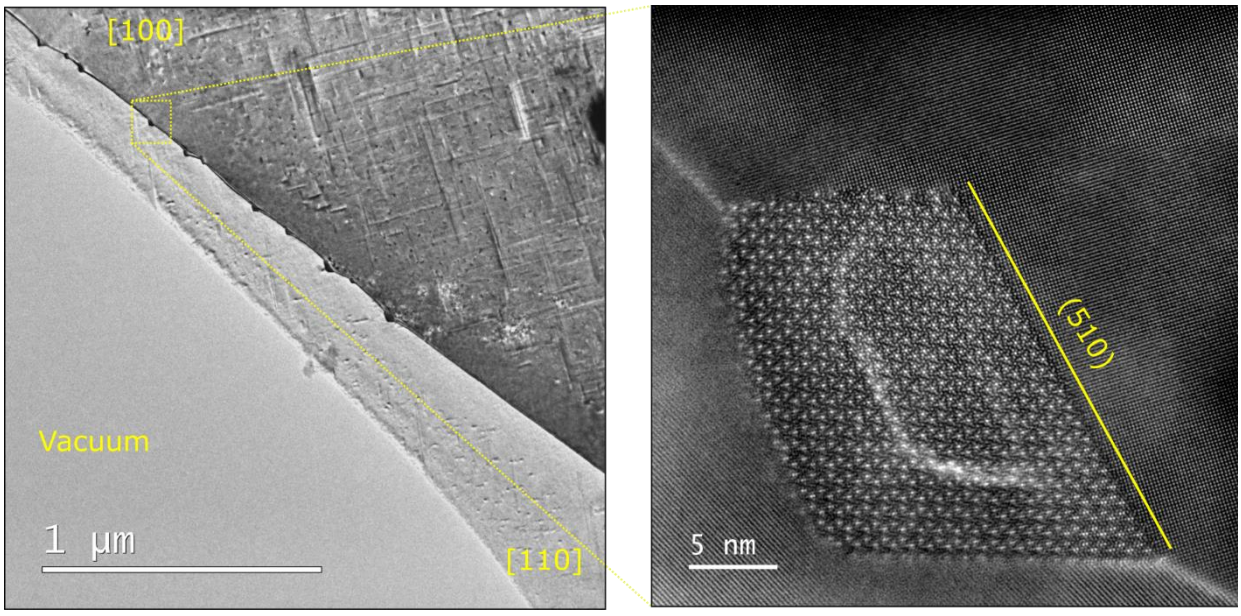

a) *BF-TEM of T7 GB.* ***b)*** *HAADF-STEM image of a Q-phase precipitate.*

Figure 4.11 AA6005 T7 grain boundary with Q-phase precipitates. All the precipitates found in a) were imaged using HAADF-STEM and found to lie on the (510) aluminium plane as shown in b).

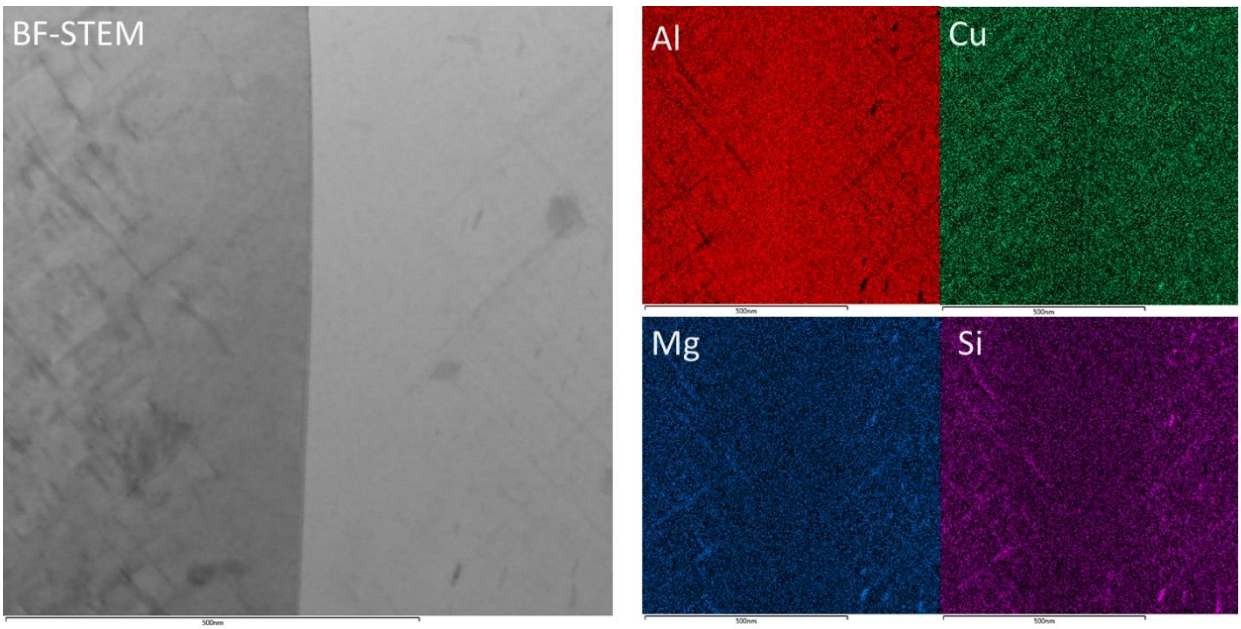

Figure 4.12 BF-STEM image and EDS map of AA6005 T7 GB. The scale bar is 500 nm.

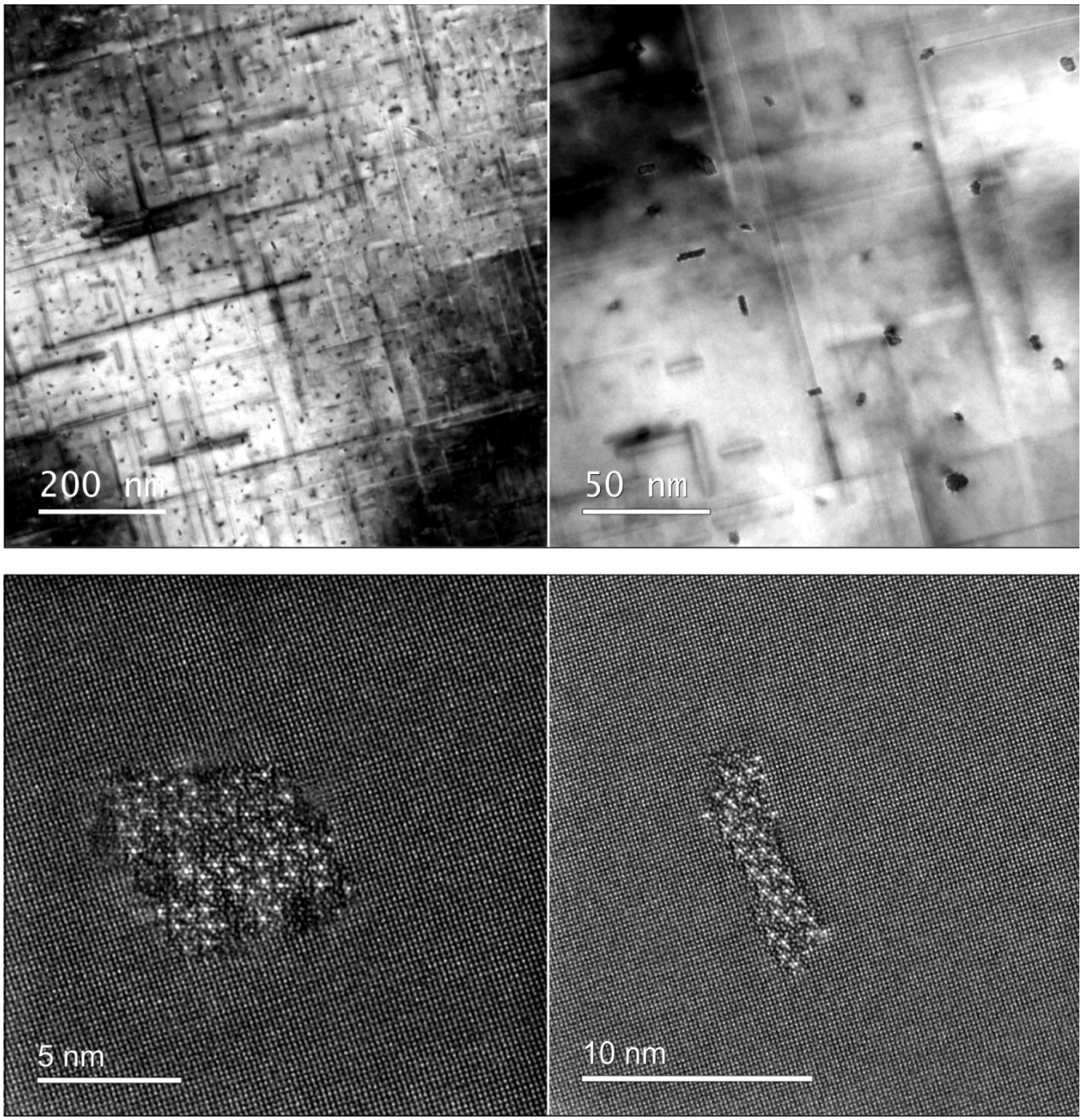

Figure 4.13 Bulk Q-phase precipitates captured with HAADF-STEM.

4.4. Vickers Hardness Measurement

The Vickers hardness of underaged (T6x), peak aged (T6) and overaged (T7) materials of both alloys were measured to verify the effect of artificial aging. Samples from the section of the extruded profile that went through air cooling (AC) after extrusion were also included to study the effect of water quenching (WQ) over air cooling on the mechanical properties. The results are plotted in Figure 4.14. AA6005.40 shows higher measured hardness compared to AA6005 in both AC and WQ condition for T6 and T7 state. T6x samples are not available for AA6005.40. The highest values measured of AA6005 was found in the WQ T6 condition as could be expected. AC samples exhibit lower hardness than WQ in general, except for T7 which show an increase compared to both AC T6 and WQ T7. T4 samples were not included as they were not artificially aged, but measured values of 49.4 and 53.6 HV1 for AC and WQ respectively.

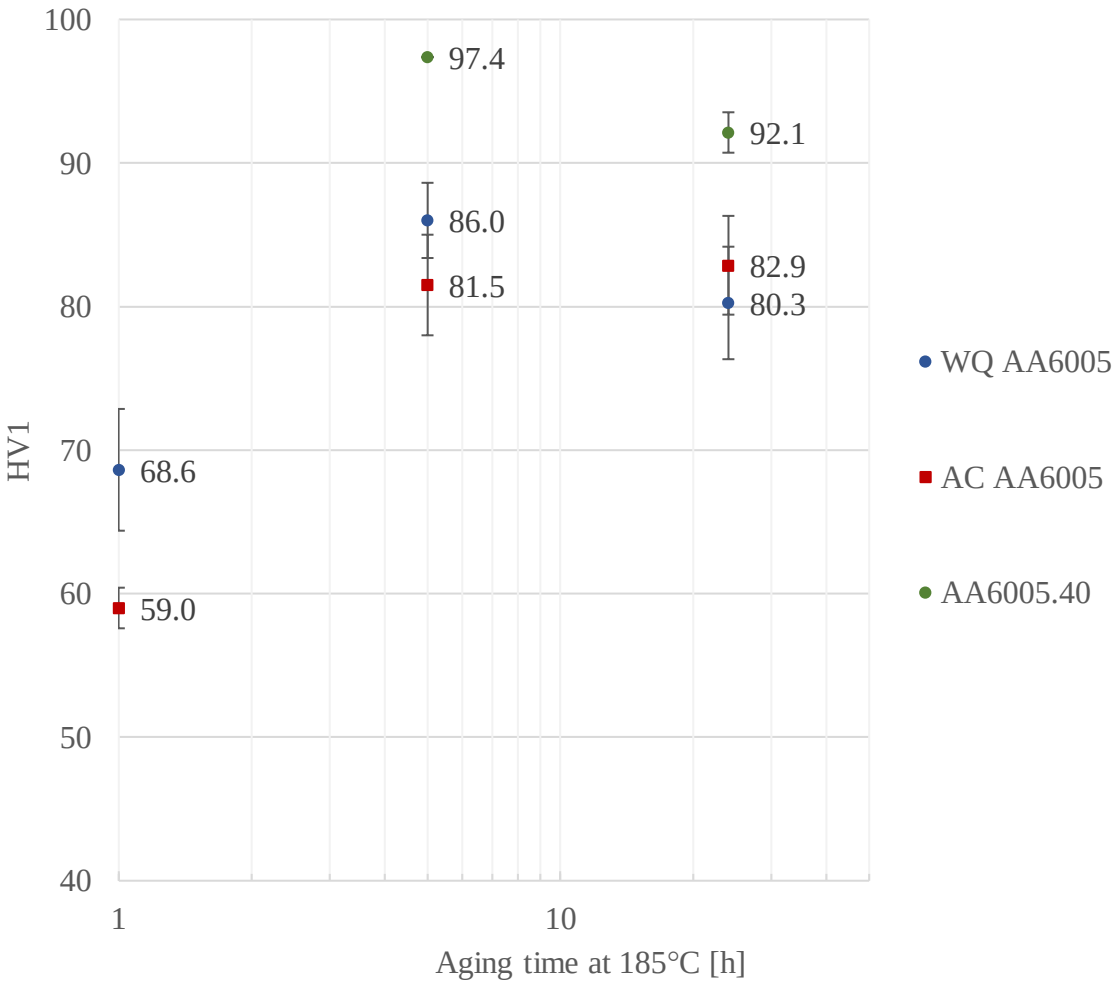

Figure 4.14 Vickers hardness versus artificial aging time. Each value is the average of eight measurements. Standard deviations are indicated with whiskers. HV1 indicates Vickers hardness measured with 1 kg load.

4.5. Accelerated Corrosion Tests

Corrosion rate and mode was recorded by weighing each sample immediately before and after accelerated IGC testing and by examining the cross section in optical microscope. Accelerated IGC tests were performed with 1 hour, 5 hours, 10, hours, 20 hours, 24 hours, 48 hours, 72 hours, 96 hours and 120 hours. The recorded mass reduction provides an indication of whether corrosion has occurred and the severity of the corrosion attack. The plot in Figure 4.15 shows the mass reduction per sample surface area as a function of the logarithm of exposure time in accelerated IGC tests.

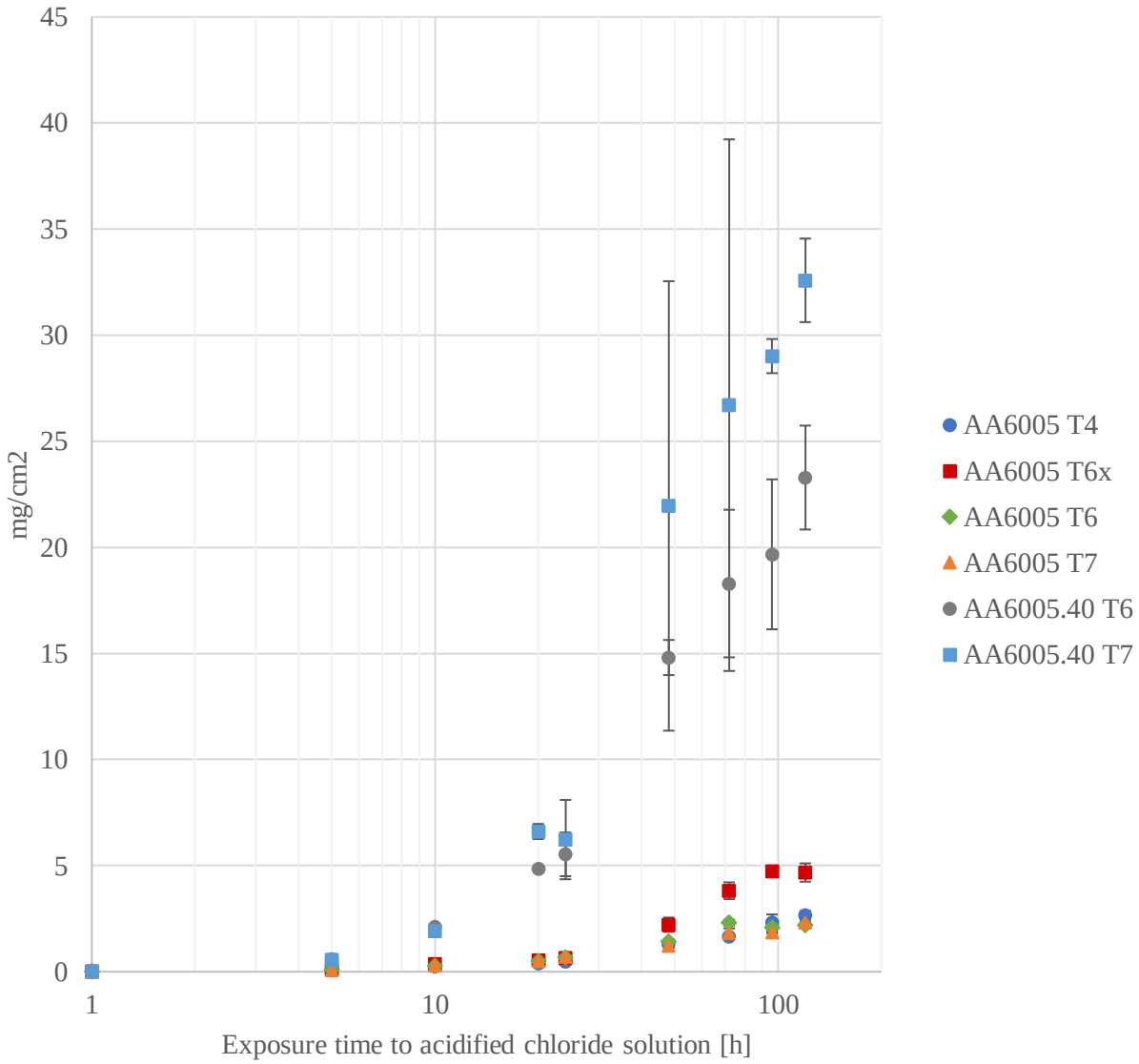

Figure 4.15 Mass reduction per sample surface area per log exposure time represented as the average of three parallels. Standard deviations are indicated with whiskers. WQ AA6005 samples were used.

It is apparent from these results that the corrosion rate of AA6005.40 is significantly higher than in AA6005 aluminium alloy. While there is little reduction in mass after one-hour exposure time for both alloys in all tempers, the difference is increasingly visible after five hours and longer. AA6005 show similar reduction in mass for all tempers up to 48 hours of exposure, where T6x temper starts to show a more rapid corrosion rate. Three parallels were used for all exposure times, whereas one parallel of each was chosen for investigation in optical microscope.

The penetration depths were determined by examining the cross-sectional micrographs and are included in Figure 4.16. The results should only be considered guiding as it represents the maximum penetration depth that was found in one cross sectional area of one of the parallels. The

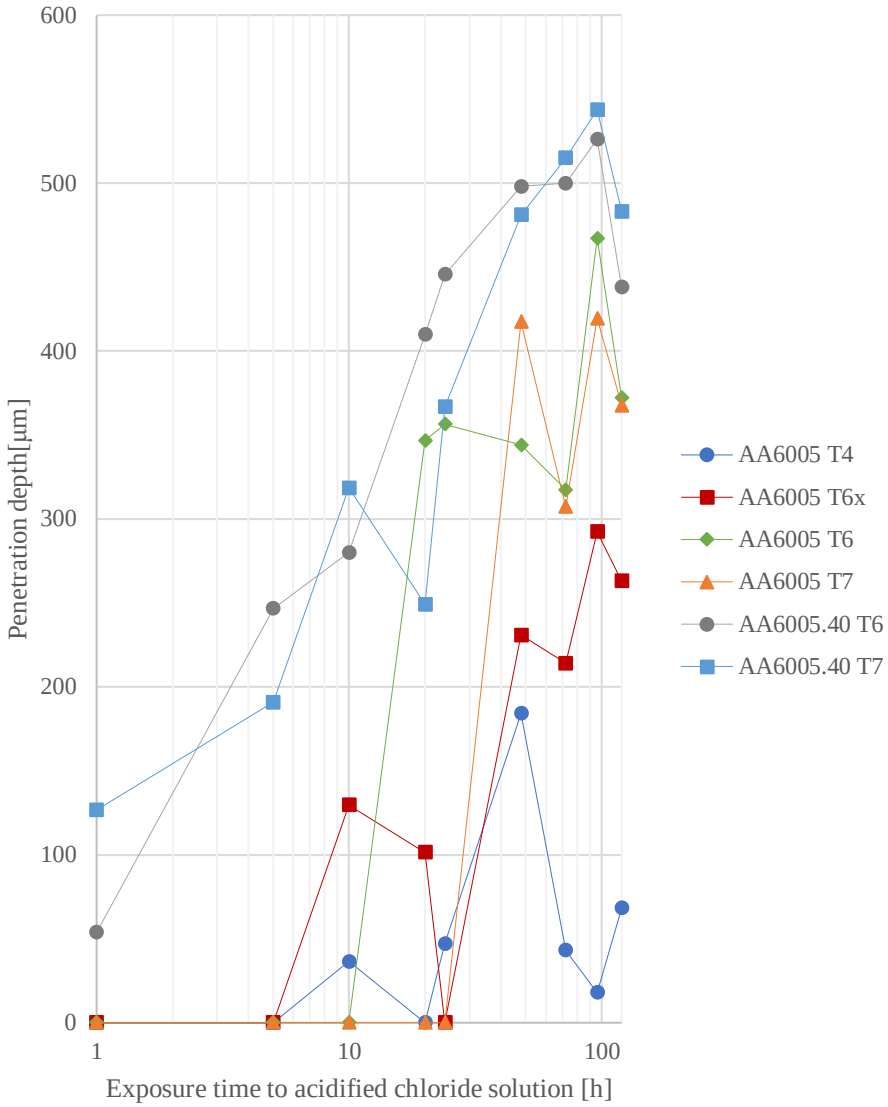

Figure 4.16 Penetration depth vs. exposure time in accelerated IGC tests for each alloy and temper. A table with exact values is included in Appendix H.

localized nature of corrosion in some tempers are reflected in the discontinuity of the measured penetration depths.

Table 4.1 lists the general corrosion mode observed. The T4 temper showed high resistance to corrosion even at 120 hours of exposure to acidified chloride solution. Some signs of etching and IGC was found, but to less extent than the other tempers. Artificial aging time altered the corrosion mode from uniform IGC at underaged (T6x) state, to localized IGC combined with pitting at peak aging (T6) and finally pitting at overaged state (T7). AA6005.40 show severe IGC in both T6 and T7 tempers even at relatively short exposure times to accelerated IGC testing.

Table 4.1 Corrosion mode observed in AA6005 and AA6005.40 for each temper.

Temper	**Dominating corrosion mode**
AA6005 T4	IGC/etching
AA6005 T6x	Uniform IGC
AA6005 T6	Localized IGC/pitting
AA6005 T7	Pitting
AA600540 reference T6	Uniform IGC
AA600540 reference T7	Uniform IGC

AA6005 T4

Samples of Fe-and Mn-reduced AA6005 that went through natural aging (T4) showed the highest corrosion resistance at all exposure times after accelerated IGC testing. Clear indications of IGC was first observed after 48 hours exposure to acidified chloride solution, while local etching of the surface was found after shorter exposure times. IGC was not found to increase at prolonged testing, while etching of the surface became more evolved. Cross sections of samples from all tests are included in Figure 4.17.

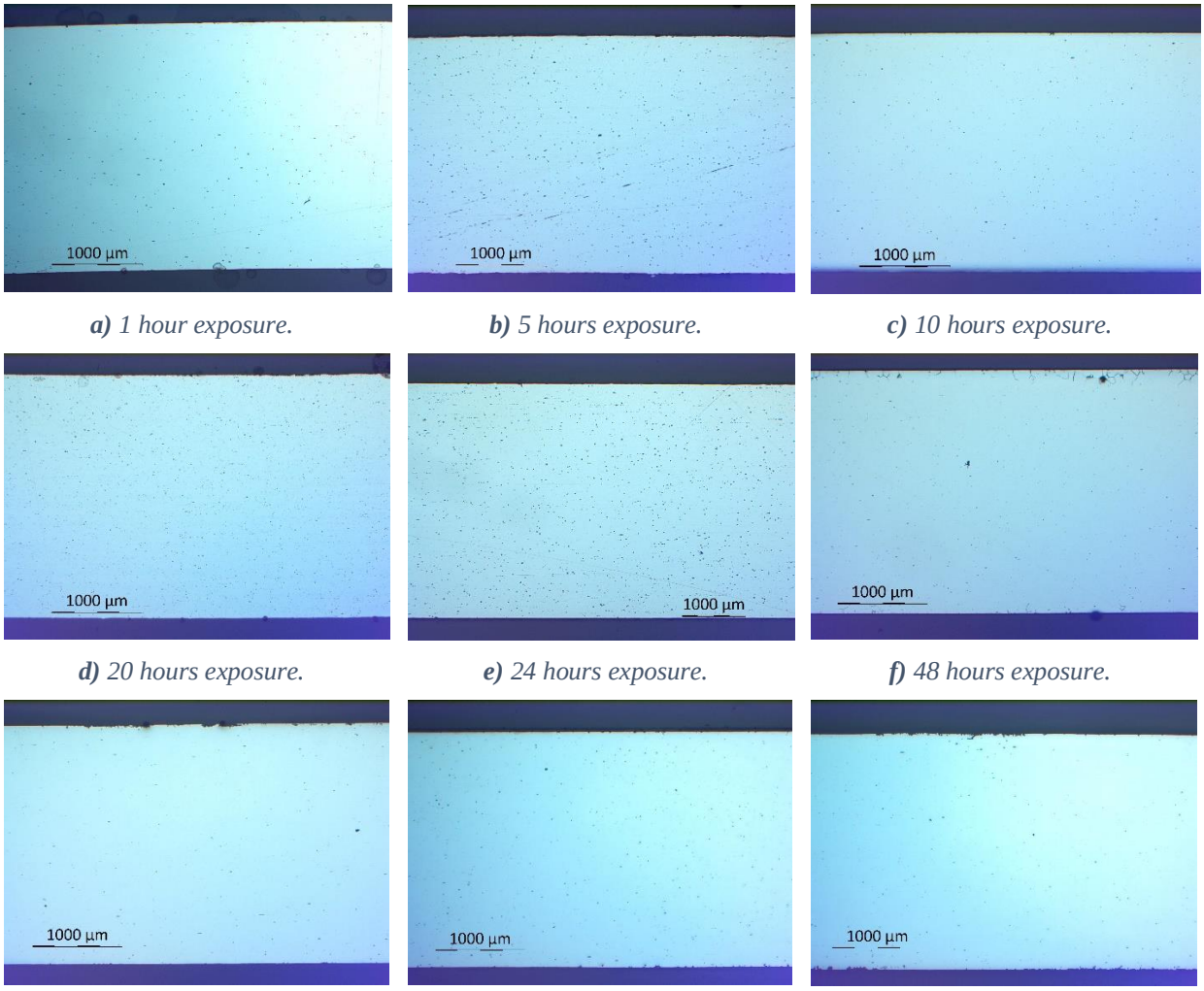

a) *1 hour exposure.* ***b)*** *5 hours exposure.* ***c)*** *10 hours exposure.*

d) *20 hours exposure.* ***e)*** *24 hours exposure.* ***f)*** *48 hours exposure.*

g) *72 hours exposure.* ***h)*** *96 hours exposure.* ***i)*** *120 hours exposure.*

Figure 4.17 Cross sections of AA6005 T4 with 25X magnification at varying exposure times to accelerated IGC testing.

Figure 4.18 shows magnified images of corroded T4 samples after 48 and 120 hours exposure. While IGC was observed after 48 hours the penetration was limited and not found in any other samples.

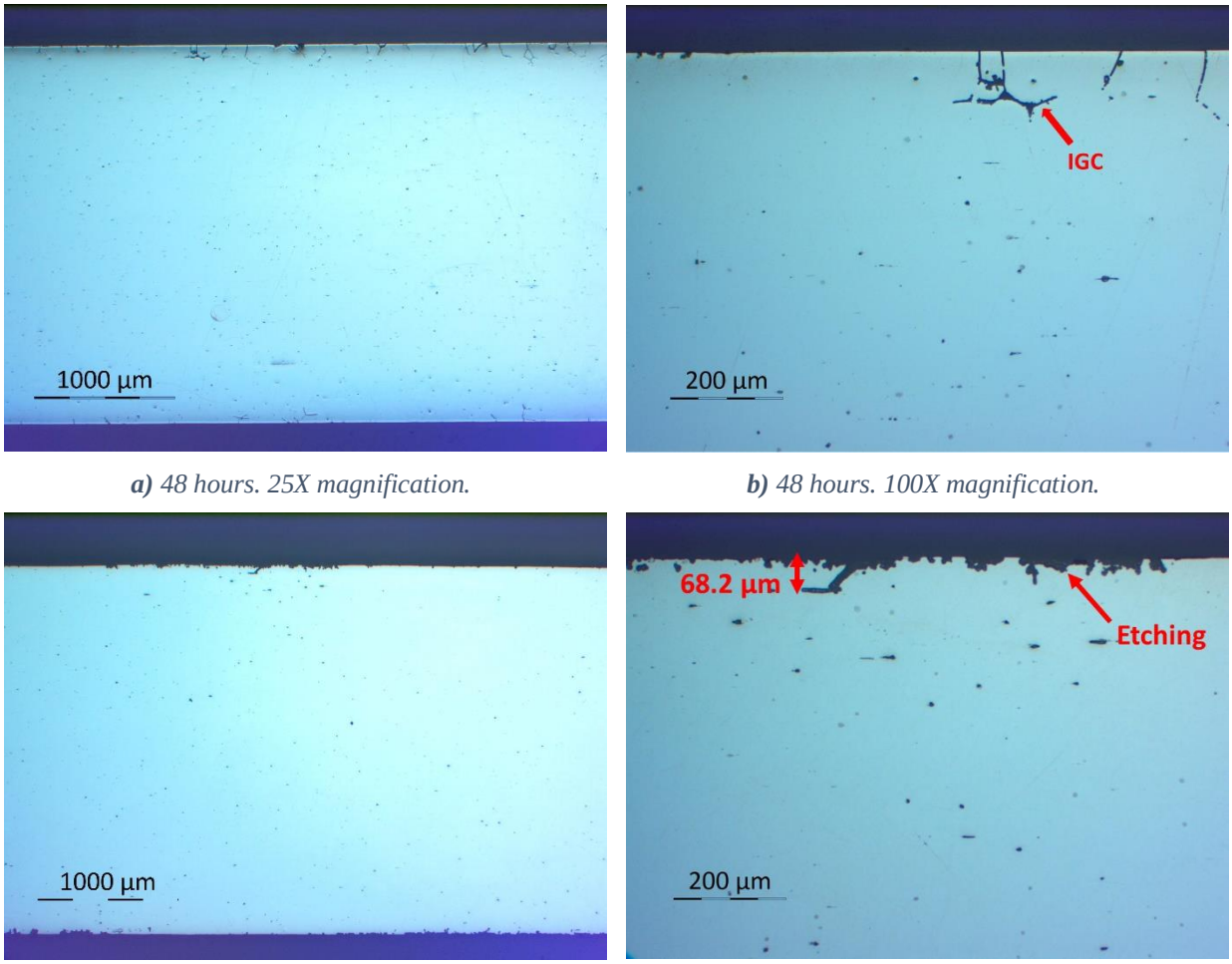

a) *48 hours. 25X magnification.*

b) *48 hours. 100X magnification.*

c) *120 hours. 25X magnification.*

d) *120 hours. 100X magnification*

Figure 4.18 IGC initiated after 48 and 120 hours of exposure to accelerated IGC tests. ***a)-b)*** *IGC initiated.* ***c)-d)*** *Local etching.*

AA6005 T6x

Initiation of IGC was found after 10 hours of accelerated IGC testing of underaged samples (T6x). At exposure times shorter than 48 hours there was limited propagation of IGC, while a significant increase was observed after 48 hours. Images captured of samples from all exposure times are included in Figure 4.19. Rapid increase in mass reduction per sample surface area after 48 hours of exposure can be explained by whole grains being removed due to IGC.

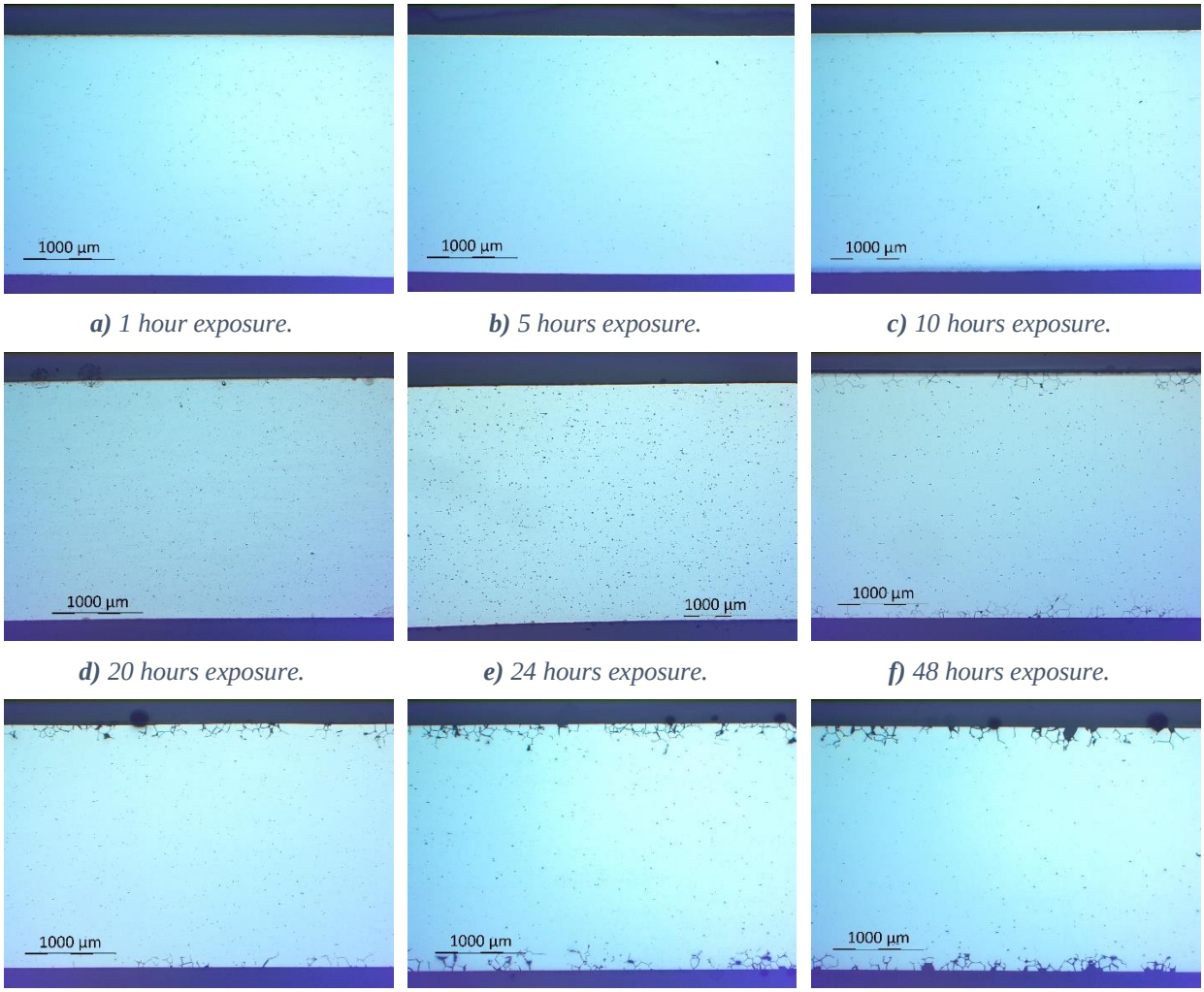

a) *1 hour exposure.* ***b)*** *5 hours exposure.* ***c)*** *10 hours exposure.*

d) *20 hours exposure.* ***e)*** *24 hours exposure.* ***f)*** *48 hours exposure.*

g) *72 hours exposure.* ***h)*** *96 hours exposure.* ***i)*** *120 hours exposure.*

Figure 4.19 Cross sections of AA6005 T6x with 25X magnification at varying exposure times to accelerated IGC testing.

Magnified images of initiation of IGC (10 hours) and max penetration depth (120h) found in AA6005 T6x is included in Figure 4.20. IGC observed after 10 hours shows a sharp line along GBs, while at 120 hours of exposure the IGC attack has coarsened.

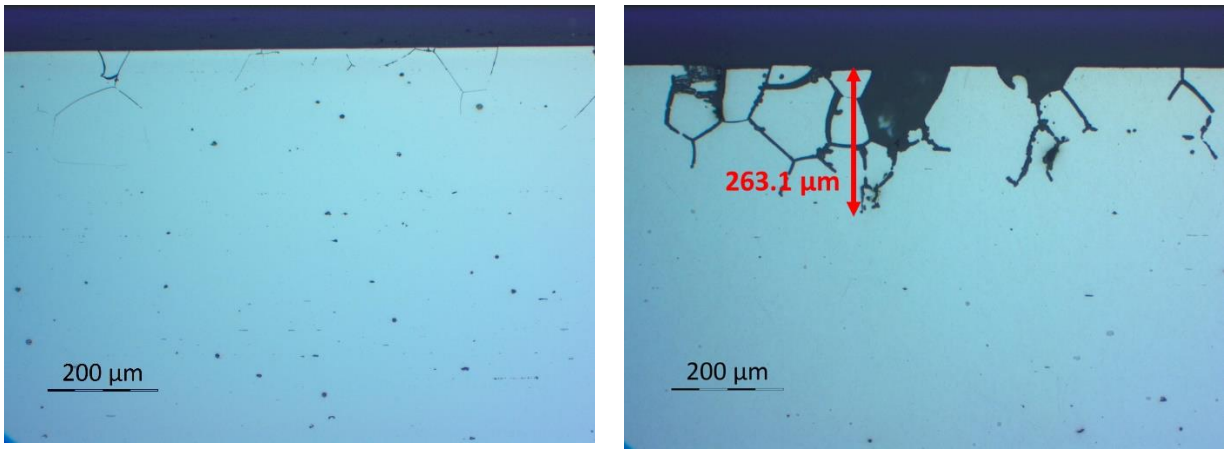

a) *10 hours. 100X magnification.* ***b)*** *120 hours. 100X magnification.*

Figure 4.20 IGC initiation and maximum exposure time of AA6005 T6x.

AA6005 T6

T6 samples of AA6005 exhibit both IGC and pitting, first observed after 5 hours immersion time. While no IGC or pitting was observed after 1 hour exposure to accelerated IGC testing, it cannot be excluded as it occurs locally and only one cross section was thoroughly investigated. However, the recorded mass reduction supports the observations in optical microscope. Prolonged immersion time resulted in lateral IGC propagation as well as coarsening of the IGC path, while penetration depths stabilized after 20 hours. Cross sections of samples from each immersion time is presented in Figure 4.21. Figure 4.22 shows samples after 48 and 120 hours at 100X magnification, which illustrates stabilization of penetration depth and coarsening of IGC.

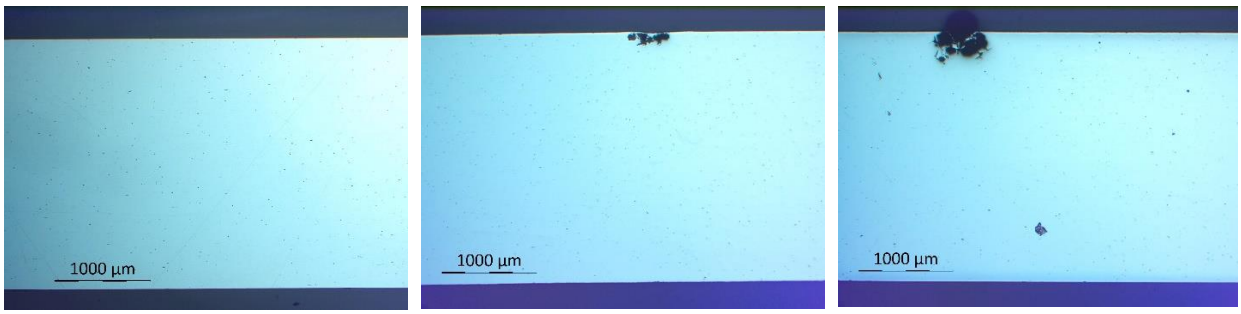

a) *1 hour exposure.* ***b)*** *5 hours exposure.* ***c)*** *10 hours exposure.*

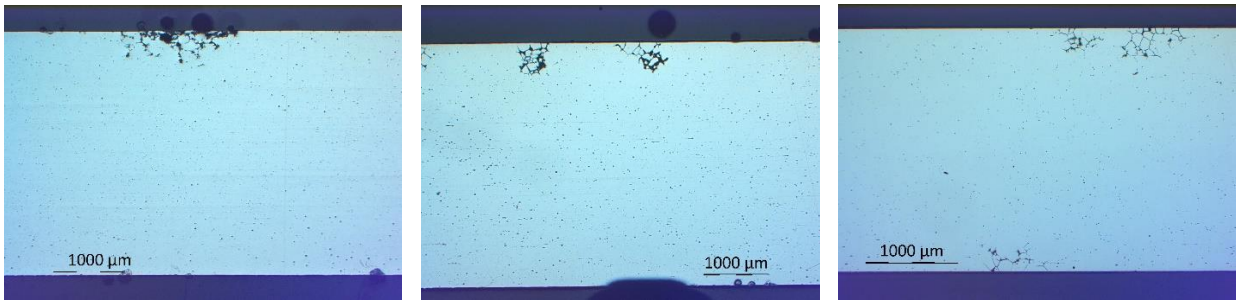

d) *20 hours exposure.* ***e)*** *24 hours exposure.* ***f)*** *48 hours exposure.*

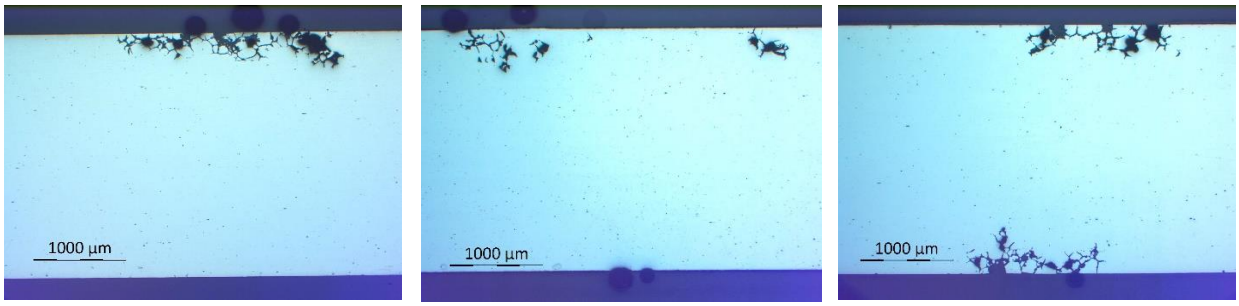

g) *72 hours exposure.* ***h)*** *96 hours exposure.* ***i)*** *120 hours exposure.*

Figure 4.21 Cross sections of AA6005 T6 with 25X magnification at varying exposure times to accelerated IGC testing.

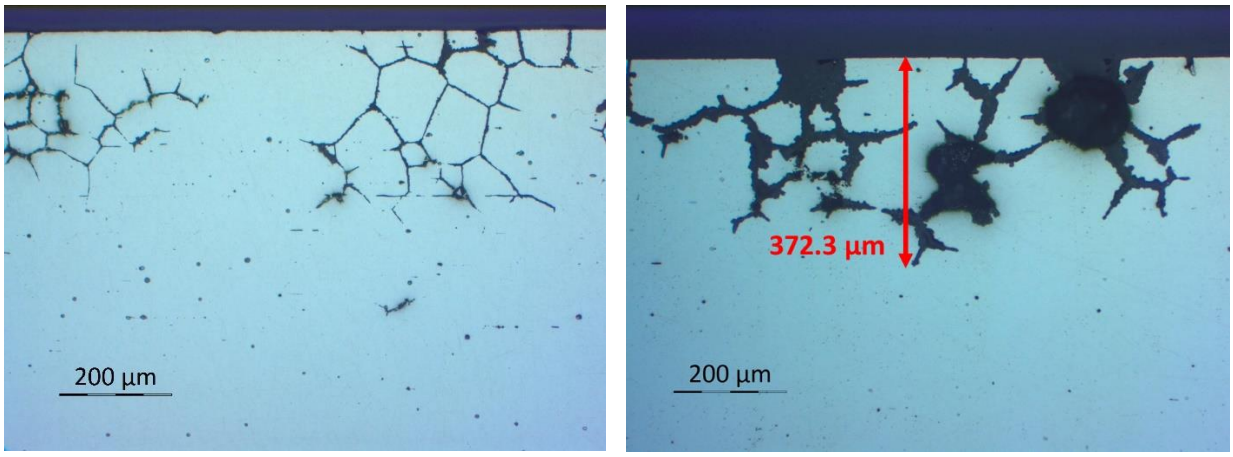

a) *48 hours. 100X magnification.* ***b)*** *120 hours. 100X magnification.*

Figure 4.22 Coarsening of IGC and pitting with prolonged exposure time to accelerated IGC tests.

AA6005 T7

Corrosion was first observed after 5 hours exposure to accelerated IGC testing for T7 tempers of the Fe- and Mn-reduced 6005 alloy. The dominating corrosion mode is pitting, while some signs of IGC is also found at shorter exposure times (5 and 24 hours). Pit size appear to somewhat

increase due to increasing immersion time, while this may be caused by local variances. Pitting was not found at 10 and 20 hours on the cross sections captured, however it is likely that pitting has occurred as corrosion is observed at shorter exposure times.

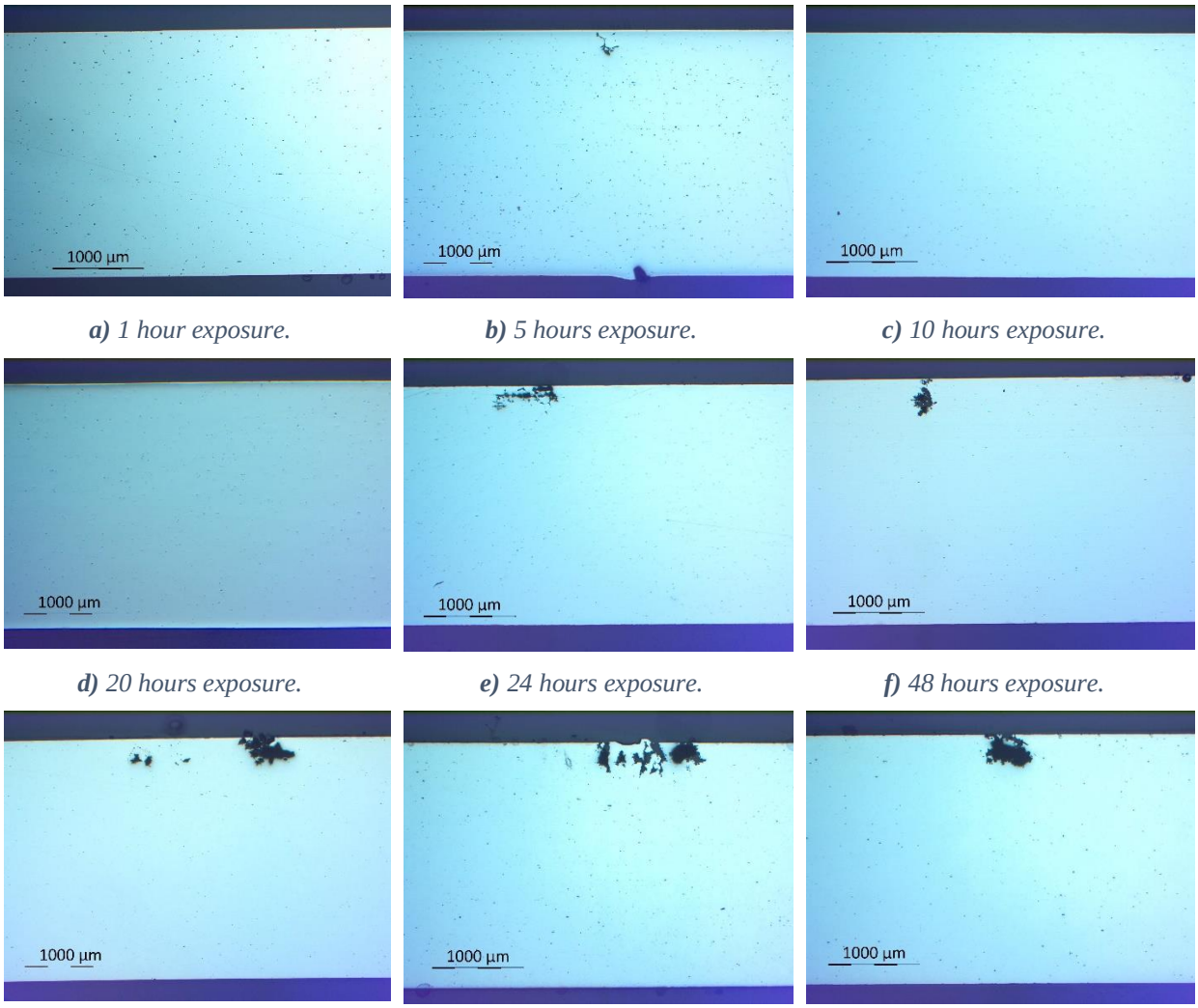

a) *1 hour exposure.* ***b)*** *5 hours exposure.* ***c)*** *10 hours exposure.*

d) *20 hours exposure.* ***e)*** *24 hours exposure.* ***f)*** *48 hours exposure.*

g) *72 hours exposure.* ***h)*** *96 hours exposure.* ***i)*** *120 hours exposure.*

Figure 4.23 Cross sections of AA6005 T7 with 25X magnification at varying exposure times to accelerated IGC testing.

AA600540 reference T6 and T7

AA6005.40 behave similarly for T6 and T7 tempers in response to accelerated IGC tests. IGC is observed already after 1 hour exposure and increase in frequency with longer exposure time up to 20 hours, where it is uniform across the surface. The dominating corrosion mode is IGC, while some small pits are found. At exposure times shorter than or equal to 15 hours the IGC is limited to the first two microstructure layers, and primarily spreads laterally. Prolonged exposure time

lead to IGC propagation into layer 3 while grains in layer 1 and 2 are removed entirely due to corrosion. IGC propagation into layer 4 was limited and did not progress significantly at prolonged exposure time. Figure 4.24 and Figure 4.25 provides an overview of propagation of IGC in respectively T6 and T7 tempers of AA600540 reference.

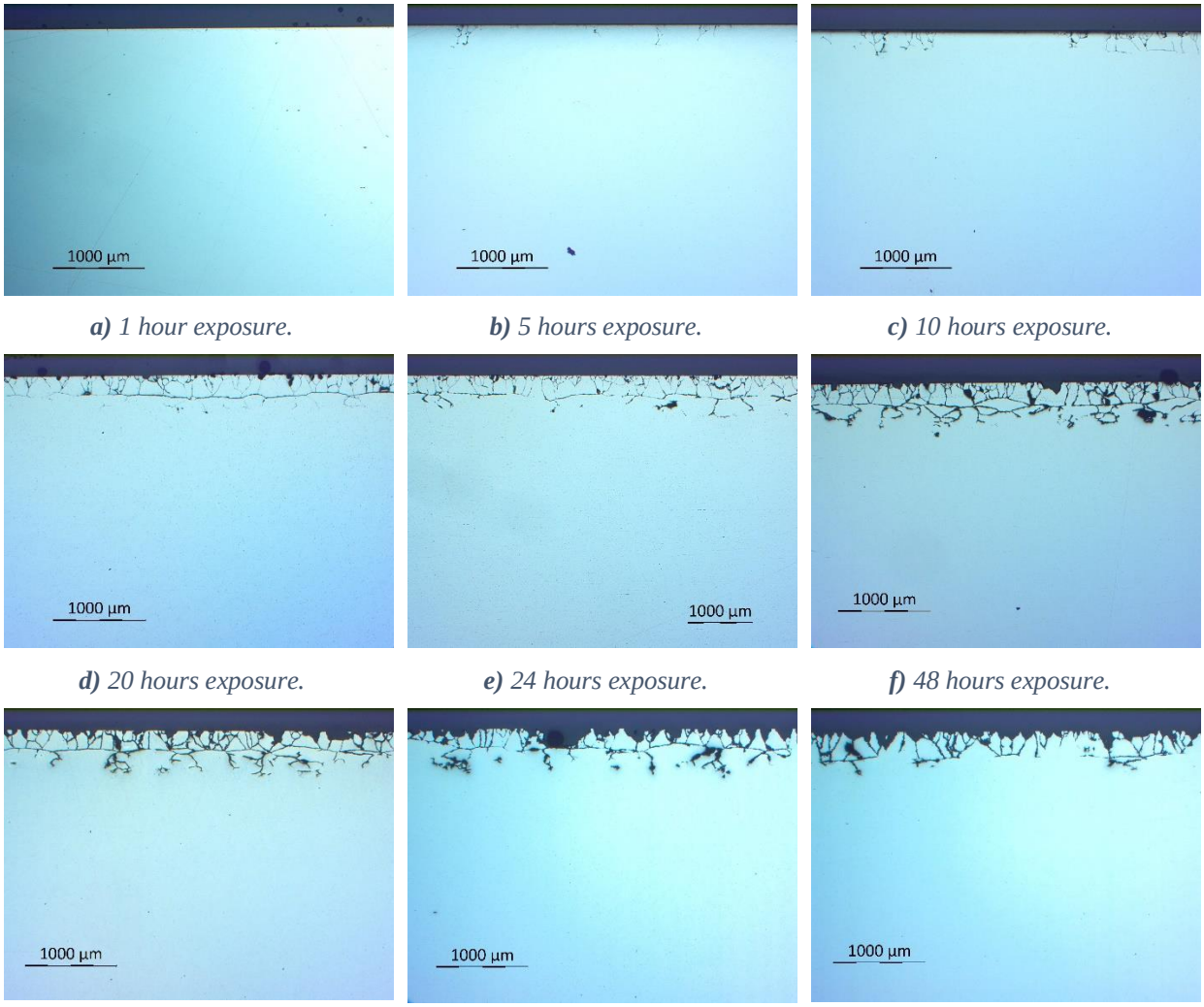

a) *1 hour exposure.* ***b)*** *5 hours exposure.* ***c)*** *10 hours exposure.*

d) *20 hours exposure.* ***e)*** *24 hours exposure.* ***f)*** *48 hours exposure.*

g) *72 hours exposure* ***h)*** *96 hours exposure* ***i)*** *120 hours exposure*

Figure 4.24 Corrosion of AA6005.40 at varying exposure times. 25X magnification.

a) *1 hour exposure.* ***b)*** *5 hours exposure.* ***c)*** *10 hours exposure.*

d) *20 hours exposure.* ***e)*** *24 hours exposure.* ***f)*** *48 hours exposure.*

g) *72 hours exposure.* ***h)*** *96 hours exposure.* ***i)*** *120 hours exposure.*

Figure 4.25 Corrosion of AA6005.40 T7 at varying exposure times. 25X magnification.

Propagation of IGC through the microstructural layers of AA6005.40 at T6 tempering is illustrated in Figure 4.26. IGC propagates rapidly through layer 1 and 2, while lateral spreading is delayed. After 20 hours faint IGC is observed in layer 3, which after 48 hours has propagated through to layer 4. T7 tempers show similar propagation but differs from T6 by higher removal rate of whole grains from layer 1 and 2 starting at 48 hours of exposure to acidified chloride solution.

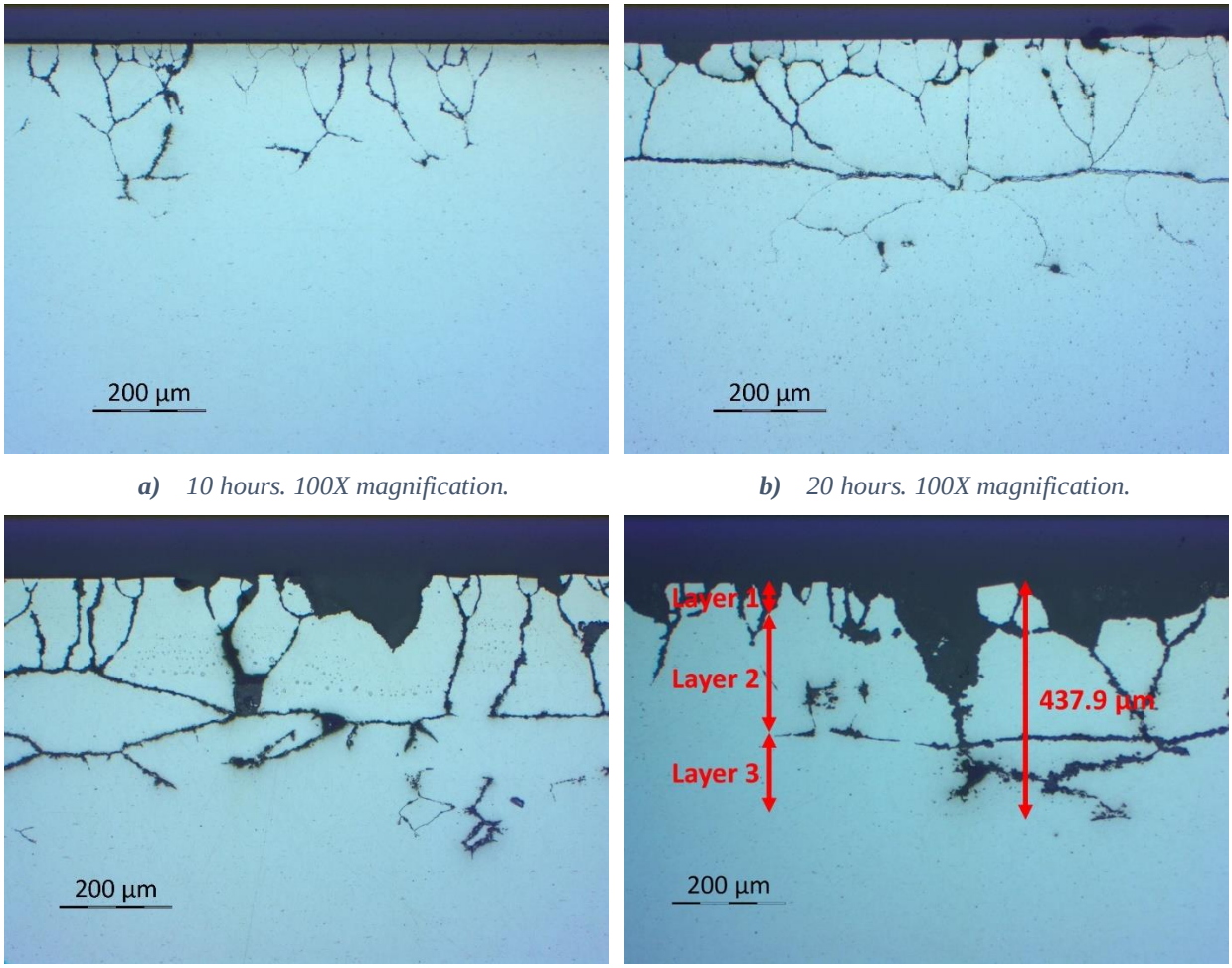

a) *10 hours. 100X magnification.*

b) *20 hours. 100X magnification.*

c) *48 hours. 100X magnification.*

d) *120 hours. 100X magnification.*

Figure 4.26 Propagation of IGC in AA6005.40T6. ***a)*** *IGC through layer 1 and 2 at 10 hours exposure.* ***b)*** *IGC propagated to layer 3 at 20 hours exposure.* ***c)*** *Developed IGC through layer 3 and into layer 4 at 48 hours exposure.* ***d)*** *Increased exposure time to 120 hours have not resulted in further propagation.*

5. Discussion

The primary objective of this thesis is to evaluate how IGC susceptibility is affected by reduced Fe-contents. Microstructural and electrochemical considerations are treated in this discussion in terms of grain size and shape, grain boundary misorientation and the presence of precipitates and Cu-film.

5.1. The Effect of Microstructure on IGC Propagation

The effect of microstructure and misorientation angles is most easily treated by comparing AA6005 T6x with AA6005.40, as they both exhibit somewhat uniform IGC across the sample surface. Optical microscopy images and EBSD analysis reveal microstructural layering in AA6005.40, while this is not seen in AA6005. Electrochemical factors and Fe-contents are also expected to influence the results.

The microstructural layers 1 and 2 in AA6005.40 show GBs perpendicular to the sample surface and elongation in the direction perpendicular to the extrusion direction. As proposed by Berneder et. al. this results in a minimized IGC path, facilitating IGC propagation through these layers (12). As observed in accelerated corrosion tests, IGC penetrates these layers within 5 to 10 hours exposure to acidified chloride solution, while lateral propagation is limited. After 20 hours of exposure, IGC has initiated on most of the surface and is severe in the first two microstructural layers. Faint indication of IGC initiation in layer 3 can also be observed. At prolonged exposure times layer 3 is penetrated by IGC and somewhat progressed into layer 4, however penetration depths appear to be mostly confined to the first three layers and does not significantly increase after 48 hours of exposure.

IGC in AA6005 T6x is limited until 48 hours of exposure. The large and more equiaxed grains result in a prolonged IGC path compared to AA6005.40, while is likely that other factors also are relevant. The penetration depth does not increase by prolonged exposure time from 96 to 120 hours. EBSD images of AA6005 T6 show a region of smaller grains with low misorientation angles at approximately 200-300 μm beneath the surface. Histograms of the normalized frequency of GB misorientations in the surface region compared to the bulk, as depicted in Figure 4.5, also suggest higher concentrations of HAGBs close to the surface and LAGBs in the bulk. Due to selective segregation to HAGBs, the region of LAGBs may act as a barrier to IGC due to reduced

availability of internal cathodes (27). EBSD imaging should be conducted of a greater area to determine whether this region of LAGBs is a local phenomenon or occurs globally in AA6005.

5.2. The Effect of Thermomechanical History

The corrosion mode in AA6005 varied with thermomechanical history, as previously found by Svenningsen et. al. (13). Naturally aged samples (T4) showed the highest corrosion resistance and clear indications of IGC was not observed until 48 hours of exposure to acidified chloride solution. While initiation occurred in multiple places on the sample surface it did not propagate deep into the sample cross section. Instead, etching was observed on the surface. The limited penetration depth may be a result of absence of internal cathodes. Examination in SEM or TEM, and EDS analysis of GBs should be conducted for verification.

Artificially underaged (T6x) samples showed initiation at several sites after 10 hours, while penetration depths and lateral spreading remained limited up until 48 hours of immersion in acidified chloride solution. Increased exposure time after 48 hours lead to faint coarsening of the IGC path and removal of surface grains, while penetration depths did not increase significantly. Cu-rich GB film, as revealed by STEM images and EDS analysis, are expected to serve as effective internal cathodes (6). Q-phase precipitates were also observed on GBs and contribute somewhat as internal cathodes. However, Kumari et. al. suggested that these where ineffective and may serve as physical barriers to IGC propagation. The presence of Cu-film explains why IGC is observed as the dominating corrosion mode, while the limited propagation may be explained by GBs free of Cu-film serving as barriers. An overview of the distribution of GB precipitates and Cu-rich GB film through the cross section may contribute to understanding the mechanisms of IGC propagation.

The distribution of misorientation angle between the surface region and bulk as plotted in Figure 4.5a indicates that a higher fraction of bulk GBs are LAGBs compared to the surface. Solute elements selectively segregate to HABGs over LAGBs and deposits as precipitates or GB-film (27, 35). It follows that the delayed propagation of IGC deeper into the cross section of AA6005 T6x may be a result of fewer GBs with available internal cathodes to sustain IGC.

T6 temper of Fe- and Mn-reduced AA6005 exhibit corrosion in the form of localized IGC and some associated pits. Initiation was found after 5 hours of exposure to acidified chloride solution in both temper conditions. STEM images and EDS analysis of grain boundary regions in T6 revealed GB precipitates and faint Cu-rich GB film. A slight rotation of the GB pictured in Figure 4.9 show selective precipitation on the certain misorientation angles and faint indications of Cu-film on the precipitate-free GB. These findings suggest local variations in the availability of effective internal cathodes, which may explain the localized IGC as observed after accelerated corrosion testing. GBs without effective internal cathodes may instead serve as barriers, limiting the spreading of corrosion.

Pitting is found in T7 tempers which first was observed after 5 hours of accelerated corrosion testing. These results comply with studies conducted by Svenningsen et al, who attributed the gradual transition from IGC to pitting at prolonged artificial aging time to coarsening of precipitates and GB film (13, 14). Prolonged exposure time to acidified chloride solution result in some increase in pit size. However, the localized nature of the corrosive attack makes it difficult to make generalizations of the development, where differences may arise due to local variations. The presence of faint Cu film and observed IGC in T6 and the absence of Cu-film in T7 along with pitting, supports the findings made by Kumari et. al. and Svenningsen et. al. stating that Cu-film is vital to sustain IGC.

5.3. Effect of Fe Content on IGC Behaviour

While varying corrosion mode in AA6005 makes it difficult to isolate the effects of Fe-content and thus availability of α-phase as initiation sites, some general trends are observed. Initiation of IGC was generally slower in AA6005 than in AA6005.40, and the corrosive attack less severe even at prolonged exposure to acidified chloride solution. The reduced Fe-content has likely resulted in fewer initiation sites, which combined with less beneficial microstructure in terms of IGC propagation has caused in improved corrosion resistance. Kumari et. al. found that not all α-particles serve as initiation sites for corrosion, which was attributed to the large stability window in terms of Fe, Mn and Cu-content (6). It is plausible that the reduced Fe- and Mn-content also has resulted in lower Fe- and Mn- concentration within the α-phase itself, thus limiting their effect as initiation sites.

Kumari et. al. also stated that α-phase indirectly continues to serve as external cathodes and thus contributes to IGC propagation even after they have corroded due to redeposited Cu that was previously incorporated in the particles. As minimal α-phase is present in AA6005 while Cu-contents are similar in both alloys, it may be relevant to discuss the distribution of Cu in the two alloys. It follows that less metallic Cu should be available as external cathodes and instead be incorporated in Q-phase, Cu-film or bulk precipitates, while this would have to be studied further.

5.4. Practical significance

Although varying with thermomechanical history, AA6005 proved to have significantly improved corrosion resistance compared to AA6005.40. The standard accelerated IGC test according to EN ISO 11846:2008 includes immersion in acidified chloride solution for 24 hours, while exposure times up to 120 hours were executed in this thesis. At 24 hours of exposure, AA6005 was practically unaffected by corrosion in T4 and T6x tempers, and while corrosion occurred in T6 and T7 tempers, the severity was significantly reduced compared to AA6005.40.

However, the purpose of alloying AlMgSi with Cu is to improve the mechanical properties of the alloy. While reduced Fe-content improved the corrosion properties, the measured Vickers Hardness was also reduced. TEM imaging of AA6005 T6 showed large Mg_2Si particles in the bulk, which may have contributed somewhat to reduced hardness as it incorporates Mg and Si that otherwise would be available to form hardening precipitates. These phases are normally dissolved during homogenization (7).

5.5. Suggestions for future work

- Due to the localized nature of corrosion in AA6005 T6 and T7, complementary SEM images of corrodes samples showing the frequency of corrosive attacks and spreading would contribute to describing the corrosion behaviour of the alloy.
- Cross-sectional BSE images of AA6005 in all tempers could help describe the GBs in terms of precipitates and Cu-film. While TEM images are presented in this thesis, BSE (SEM) images would provide information of a larger area.

- BSE images of AA6005 accompanied with EDS analysis in SEM would provide information of the availability of α-Al(Fe, Mn)Si-particles as external cathodes.
- Short-time accelerated IGC tests with multiple exposure times between 1 and 10 hours would help determining the exact initiation time of corrosion in AA6005.

6. Conclusion

- While varying with thermomechanical history, resistance to IGC was significantly improved in AA6005 compared to AA600540. Both initiation and propagation were delayed in the AA6005 alloy. This demonstrates the findings made by Kumari et. al. related to the significance of Fe on IGC initiation in AlMgSi alloys.
- Delayed propagation was attributed to microstructural as well as electrochemical considerations. AA6005 may exhibit prolonged IGC path due to more equiaxed grains near the surface. Lower frequency of effective external cathodes in the form of α-phase and residual Cu is also proposed as an explanation.
- The corrosion mode was altered as a result of increased artificial aging time, similarly to results observed by Svenningsen et. al. Artificial under aging lead to uniform IGC, while prolonged aging time to peak and over aged state lead to localized IGC and eventually pitting.
- Both AA6005 and AA6005.40 showed insignificant increases in penetration depth as a result of prolonged exposure to acidified chloride solution above 96 hours at the longest. This was attributed to lower frequency of HAGBs within the bulk and resulting reduction in available internal cathodes.

References

1. W. S. Miller, L. Zhuang, J. Bottema, A. J. Wittebrood, P. De Smet, A. Haszler, et al. Recent development in aluminium alloys for the automotive industry. Materials Science & Engineering A. 2000;280(1):37-49.

2. G. E. Totten, D. S. MacKenzie. Handbook of aluminum : Vol. 2 : Alloy production and materials manufacturing. New York: Marcel Dekker; 2003.

3. Bardal E. Korrosjon og Korrosjonsvern. Trondheim: Tapir; 1994.

4. J. G. Kaufman. Corrosion of Aluminum and Aluminum Alloys. 2005. 95-124 p.

5. M. H. Larsen, J. C. Walmsley, O. Lunder, K. Nisancioglu. Effect of excess silicon and small copper content on intergranular corrosion of 6000-series aluminum alloys. Journal of the Electrochemical Society. 2010;157(2):C61-C8.

6. S. Kumari, S. Wenner, J. C. Walmsley, O. Lunder, K. Nisancioglu. Progress in Understanding Initiation of Intergranular Corrosion on AA6005 Aluminum Alloy with Low Copper Content (Book review). Journal of The Electrochemical Society. 2019;166(11):C3114-C23.

7. O. Reiso. Extrusion of AlMgSi Alloys. Materials Forum. 2004;28.

8. S. K. Kairy, P. A. Rometsch, C. H. J. Davies, N. Birbilis. On the Intergranular Corrosion and Hardness Evolution of 6xxx Series Al Alloys as a Function of Si:Mg Ratio, Cu Content, and Aging Condition. Corrosion. 2017;73(10):1280-95.

9. S. Kumari. Initiation and propagation of intergranular corrosion on AA6005 aluminium alloy. Trondheim: Norwegian University of Science and Technology, Faculty of Natural Sciences, Department of Materials Science and Engineering; 2018.

10. G. Svenningsen, J. E. Lein, A. Bjørgum, J. H. Nordlien, Y. Yu, K. Nisancioglu. Effect of low copper content and heat treatment on intergranular corrosion of model AlMgSi alloys. Corrosion Science. 2006;48(1):226-42.

11. G. Svenningsen. Intergranular corrosion of AA6000-series aluminium alloys. Trondheim: Norwegian University of Science and Technology, Faculty of Natural Sciences and Technology, Department of Materials Technology; 2005.

12. J. Berneder, R. Rachlitz, C. Melzer, H. Antrekowitsch, P. Uggowitzer. Influence of the grain size on the IGC, crack propagation and fracture toughness behaviour of AA2024-T3 sheet material. TMS 2010 139th Annual Meeting and Exhibition - Supplemental Proceedings, Volume 1 - Materials Processing and Properties. TMS (The Minerals, Metals & Materials Society); 2010. 31-9 p.

13. G. Svenningsen, M. H. Larsen, J. C. Walmsley, J. H. Nordlien, K. Nisancioglu. Effect of artificial aging on intergranular corrosion of extruded AlMgSi alloy with small Cu content. Corrosion Science. 2006;48(6):1528-43.

14. G. Svenningsen, M. H. Larsen, J. H. Nordlien, K. Nisancioglu. Effect of thermomechanical history on intergranular corrosion of extruded AlMgSi(Cu) model alloy. Corrosion Science. 2006;48(12):3969-87.

15. M. J. Robinson, Jackson. NC. The influence of grain structure and intergranularcorrosion rate on exfoliation and stress corrosion crackingof high strength Al–Cu–Mg alloys. Corrosion Science. 1999;41(5):1013-28.

16. S. Zhao, D. A. Wolfe, T-S. Huang, G. S. Frankel. Generalized model for IGC growth in aluminum alloys. Journal of Statistical Planning and Inference. 2007;137(7):2405-12.

17. C. Marioara, A. Lervik, J. Grønvold, O. Lunder, S. Wenner, T. Furu, et al. The Correlation Between Intergranular Corrosion Resistance and Copper Content in the Precipitate Microstructure in an AA6005A Alloy. Metallurgical and Materials Transactions A. 2018;49(10):5146-56.

18. J. C. Bailey, F. C. Porter, A. W. Pearson, R. A. Jarman. Aluminium and Aluminium Alloys 2013. 4:3-37 p.

19. J. Hatch. Aluminum: Properties and Physical Metallurgy. American Society for Metals, Metals Park, Ohio 44073, USA , 1984 424 pp. 1984:424.

20. L. F. Mondolfo. Aluminum alloys : structure and properties. London: Butterworths; 1976.

21. M. H. Larsen. Effect of composition and thermomechanical processing on the intergranular corrosion of AA6000 aluminium alloys. Trondheim: Norwegian University of Science and Technology, Faculty of Natural Sciences and Technology, Department of Materials Science and Engineering; 2010.

22. S. Ji, W. Yang, F. Gao, D. Watson, Z. Fan. Effect of iron on the microstructure and mechanical property of Al–Mg–Si–Mn and Al–Mg–Si diecast alloys. Materials Science & Engineering A. 2013;564(C):130-9.

23. Aluminum Alloy 6005A - T6 Extrusion: Aalco Metals Ltd; [

24. M. Bayat, T. Carlberg, M. Cieslar. In-situ study of phase transformations during homogenization of 6005 and 6082 Al alloys. Journal of Alloys and Compounds. 2017;725:504-9.

25. M. B. Karamiş, A. Halici. The effects of homogenization and recrystallization heat treatments on low-grade cold deformation properties of AA 6063 aluminum alloy. Materials Letters. 2007;61(4 5):944.

26. P. Saha. Aluminum Extrusion Technology. Aluminum Extrusion Technology. 2000:259.

27. W. D. Callister, D. G. Rethwisch. Materials science and engineering. 9th ed., SI Version. ed. Hoboken, N.J: Wiley; 2015.

28. T. Furu, H. E. Vatne. Grain structure control of flat extruded AA6082 alloy. Aluminium Alloys: Their Physical And Mechanical Properties, Pts 1-3. 2000;331-3:843-8.

29. R. E. Smallman, A. H. W. Ngan. Modern physical metallurgy. Oxford, UK: Butterworth-Heinemann; 2014.

30. J. C. Benedyk. International temper designation systems for wrought aluminum alloys: Part II -Thermally treated (T temper) aluminum alloys. Light Metal Age. 2010.

31. C. D. Marioara, S. J. Andersen, T. N. Stene, H. Hasting, J. Walmsley, A. T. J. Van Helvoort, et al. The effect of Cu on precipitation in Al–Mg–Si alloys. Philosophical Magazine. 2007;87(23):3385-413.

32. R.Davis J. Corrosion of Aluminum and Aluminum Alloys: ASM International; 1999.

33. S. K. Kairy, T. Alam, P. A. Rometsch, C. H. J. Davies, R. Banerjee, N. Birbilis. Understanding the Origins of Intergranular Corrosion in Copper-Containing Al-Mg-Si Alloys. Metallurgical and Materials Transactions A. 2016;47(3):985-9.

34. V. Guillaumin, G. Mankowski. Influence of overaging treatment on localized corrosion on Al 6056. Corrosion. 2000;56(1):12.

35. J. Yan, N. M. Heckman, L. Velasco, Hodge AM. Improve sensitization and corrosion resistance of an Al-Mg alloy by optimization of grain boundaries. Scientific Reports. 2016;6(1).

36. J. Li, F. Li, X. Ma, J. Li, S. Liang. Effect of grain boundary characteristic on intergranular corrosion and mechanical properties of severely sheared Al-Zn-Mg-Cu alloy. Materials Science & Engineering A. 2018;732:53-62.

37. R. Zhang, R. K. Gupta, C. H. J. Davies, A. M. Hodge, M. Tort, K. Xia, et al. The influence of grain size and grain orientation on sensitization in AA5083. Corrosion. 2016;72(2):160-8.

38. E. A. Blomlie, T. Furu, O. Lunder. Intergranulær korrosjon som følge av mekanisk og termisk prosessering av ekstruderte AlMgSi(Cu)-legeringer (KK13). NTNU; 2016.

39. Huang T-S, S. Zhao, G. S. Frankel, D. Wolfe. A Statistical Model for Localized Corrosion in 7xxx Aluminum Alloys. Corrosion. 2007;63(9):819-27.

40. D. McLean. Grain boundaries in metals. Oxford: Clarendon Press; 1957.

41. R. Ambat, A. J. Davenport, G. M. Scamans, A. Afseth. Effect of iron-containing intermetallic particles on the corrosion behaviour of aluminium. Corrosion Science. 2006;48(11):3455-71.

42. H. Tanihata, T. Sugawara, K. Matsuda, S. Ikeno. Effect of casting and homogenizing treatment conditions on the formation of Al–Fe–Si intermetallic compounds in 6063 Al–Mg–Si alloys. Journal of Materials Science. 1999;34(6):1205-10.

43. D. J. Chakrabarti, D. E. Laughlin. Phase relations and precipitation in Al–Mg–Si alloys with Cu additions. Progress in Materials Science. 2004;49(3):389-410.

44. A. K. Gupta, D. J. Lloyd, S. A. Court. Precipitation hardening in Al–Mg–Si alloys with and without excess Si. Materials Science & Engineering A. 2001;316(1):11-7.

45. Y. Tamura, T. Haitani, N. Kono. Liquid Solubility of Manganese and Its Influence on Grain Size of Mg-Al Alloys. MATERIALS TRANSACTIONS. 2006;47(8):1968-74.

46. P. W. Hawkes, J. C. H. Spence. Science of Microscopy. New York, NY: New York, NY: Springer New York; 2007.

47. J. K. Solberg, V. Hansen. Innføring i Transmisjon Elektronmikroskopi 2014. 54 p.

48. D. B. Williams, C. B. Carter. Transmission electron microscopy : a textbook for materials science. 2nd ed. ed. New York: Springer; 2009.

49. M. M. J. Treacy. Z Dependence of Electron Scattering by Single Atoms into Annular Dark-Field Detectors. Microsc Microanal. 2011;17(6):847-58.

50. Standard Test Methods for Determining Average Grain Size. https://compass.astm.org: International.

51. Tømmerdal M. The Effect of Microstructure and Cu Content on Corrosion Behavior of 6060 Aluminum Alloy [Master's Thesis]: Norwegian University Of Science and Technoogy; 2018.

52. Vickers hardness. 2019. Encyclopedia Britannica, Inc.

Appendix A

Billet Characterization

Cross-section of a disc cut from the billet as etched in NaOH for 1 minute.

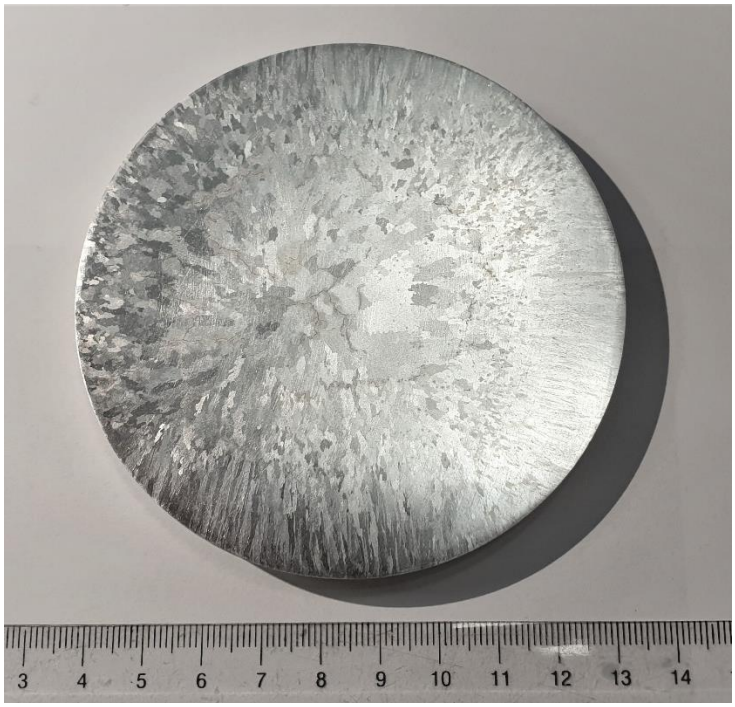

Measured Vickers Hardness 1 kg load									Avg.	Std. dev.
Measured value (HV1)	52	48	47	47	47	48	50	46	48.1	1.96

Measured Electrical Conductivity									Avg.	Std. dev.
Measured Value (MS/m)	34.6	35.3	35.2	35.0	34.7	35.0	35.0	33.9	34.8	0.46

Appendix B

Optical Emission Spectrometry of AA6005

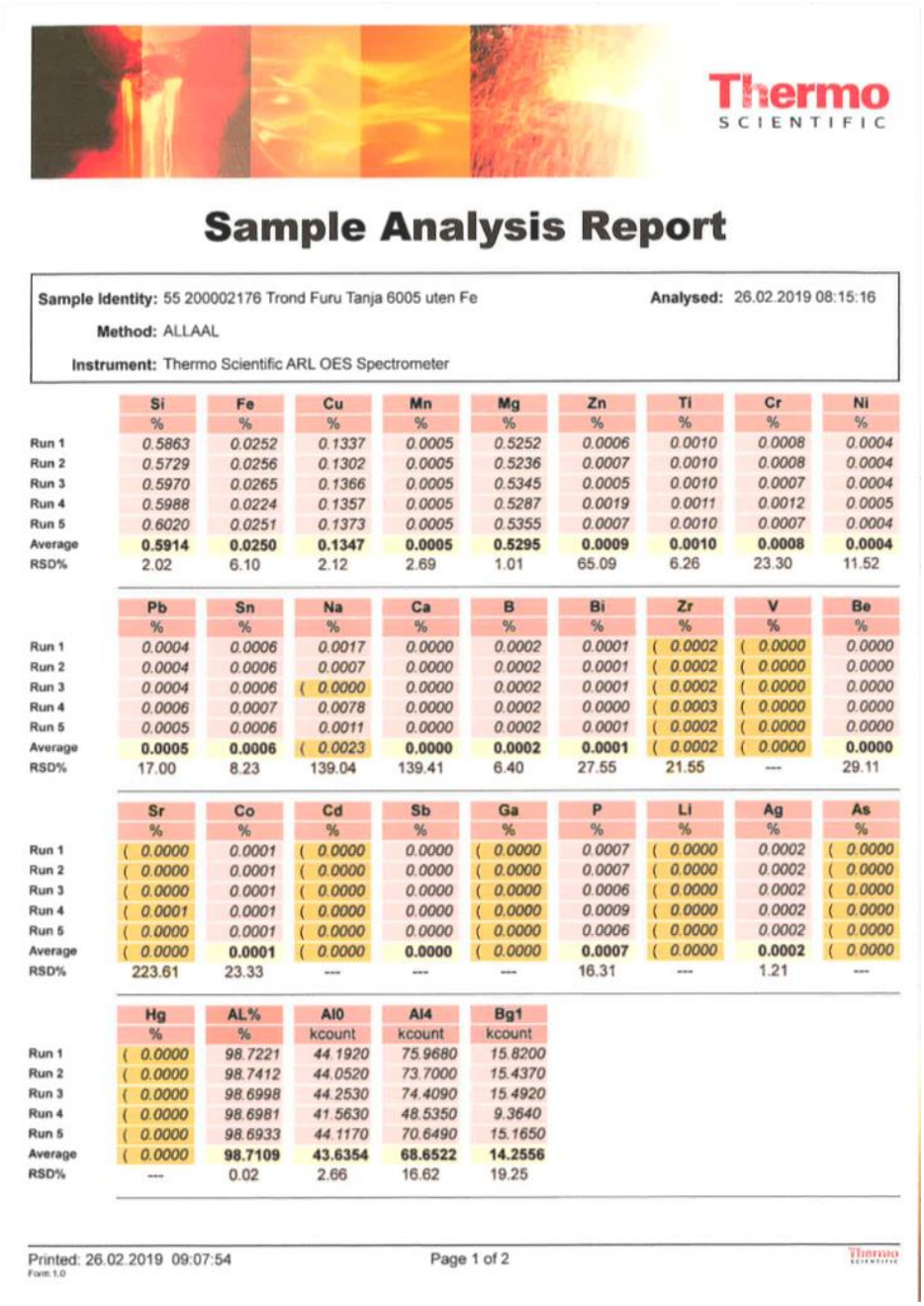

Thermo SCIENTIFIC

Sample Analysis Report

Sample Identity: 55 200002176 Trond Furu Tanja 6005 uten Fe **Analysed:** 26.02.2019 08:15:16

Method: ALLAAL

Instrument: Thermo Scientific ARL OES Spectrometer

	Si	Fe	Cu	Mn	Mg	Zn	Ti	Cr	Ni
	%	%	%	%	%	%	%	%	%
Run 1	0.5863	0.0252	0.1337	0.0005	0.5252	0.0006	0.0010	0.0008	0.0004
Run 2	0.5729	0.0256	0.1302	0.0005	0.5236	0.0007	0.0010	0.0008	0.0004
Run 3	0.5970	0.0265	0.1366	0.0005	0.5345	0.0005	0.0010	0.0007	0.0004
Run 4	0.5988	0.0224	0.1357	0.0005	0.5287	0.0019	0.0011	0.0012	0.0005
Run 5	0.6020	0.0251	0.1373	0.0005	0.5355	0.0007	0.0010	0.0007	0.0004
Average	**0.5914**	**0.0250**	**0.1347**	**0.0005**	**0.5295**	**0.0009**	**0.0010**	**0.0008**	**0.0004**
RSD%	2.02	6.10	2.12	2.69	1.01	65.09	6.26	23.30	11.52

	Pb	Sn	Na	Ca	B	Bi	Zr	V	Be
	%	%	%	%	%	%	%	%	%
Run 1	0.0004	0.0006	0.0017	0.0000	0.0002	0.0001	(0.0002	(0.0000	0.0000
Run 2	0.0004	0.0006	0.0007	0.0000	0.0002	0.0001	(0.0002	(0.0000	0.0000
Run 3	0.0004	0.0006	(0.0000	0.0000	0.0002	0.0001	(0.0002	(0.0000	0.0000
Run 4	0.0006	0.0007	0.0078	0.0000	0.0002	0.0000	(0.0003	(0.0000	0.0000
Run 5	0.0005	0.0006	0.0011	0.0000	0.0002	0.0001	(0.0002	(0.0000	0.0000
Average	**0.0005**	**0.0006**	(0.0023	**0.0000**	**0.0002**	**0.0001**	(0.0002	(0.0000	**0.0000**
RSD%	17.00	8.23	139.04	139.41	6.40	27.55	21.55	---	29.11

	Sr	Co	Cd	Sb	Ga	P	Li	Ag	As
	%	%	%	%	%	%	%	%	%
Run 1	(0.0000	0.0001	(0.0000	0.0000	(0.0000	0.0007	(0.0000	0.0002	(0.0000
Run 2	(0.0000	0.0001	(0.0000	0.0000	(0.0000	0.0007	(0.0000	0.0002	(0.0000
Run 3	(0.0000	0.0001	(0.0000	0.0000	(0.0000	0.0006	(0.0000	0.0002	(0.0000
Run 4	(0.0001	0.0001	(0.0000	0.0000	(0.0000	0.0009	(0.0000	0.0002	(0.0000
Run 5	(0.0000	0.0001	(0.0000	0.0000	(0.0000	0.0006	(0.0000	0.0002	(0.0000
Average	(0.0000	**0.0001**	(0.0000	**0.0000**	(0.0000	**0.0007**	(0.0000	**0.0002**	(0.0000
RSD%	223.61	23.33	---	---	---	16.31	---	1.21	---

	Hg	AL%	Al0	Al4	Bg1
	%	%	kcount	kcount	kcount
Run 1	(0.0000	98.7221	44.1920	75.9680	15.8200
Run 2	(0.0000	98.7412	44.0520	73.7000	15.4370
Run 3	(0.0000	98.6998	44.2530	74.4090	15.4920
Run 4	(0.0000	98.6981	41.5630	48.5350	9.3640
Run 5	(0.0000	98.6933	44.1170	70.6490	15.1650
Average	(0.0000	**98.7109**	**43.6354**	**68.6522**	**14.2556**
RSD%	---	0.02	2.66	16.62	19.25

Printed: 26.02.2019 09:07:54 Page 1 of 2

Form 1.0

Appendix C

Optical Emission Spectrometry of AA6005.40

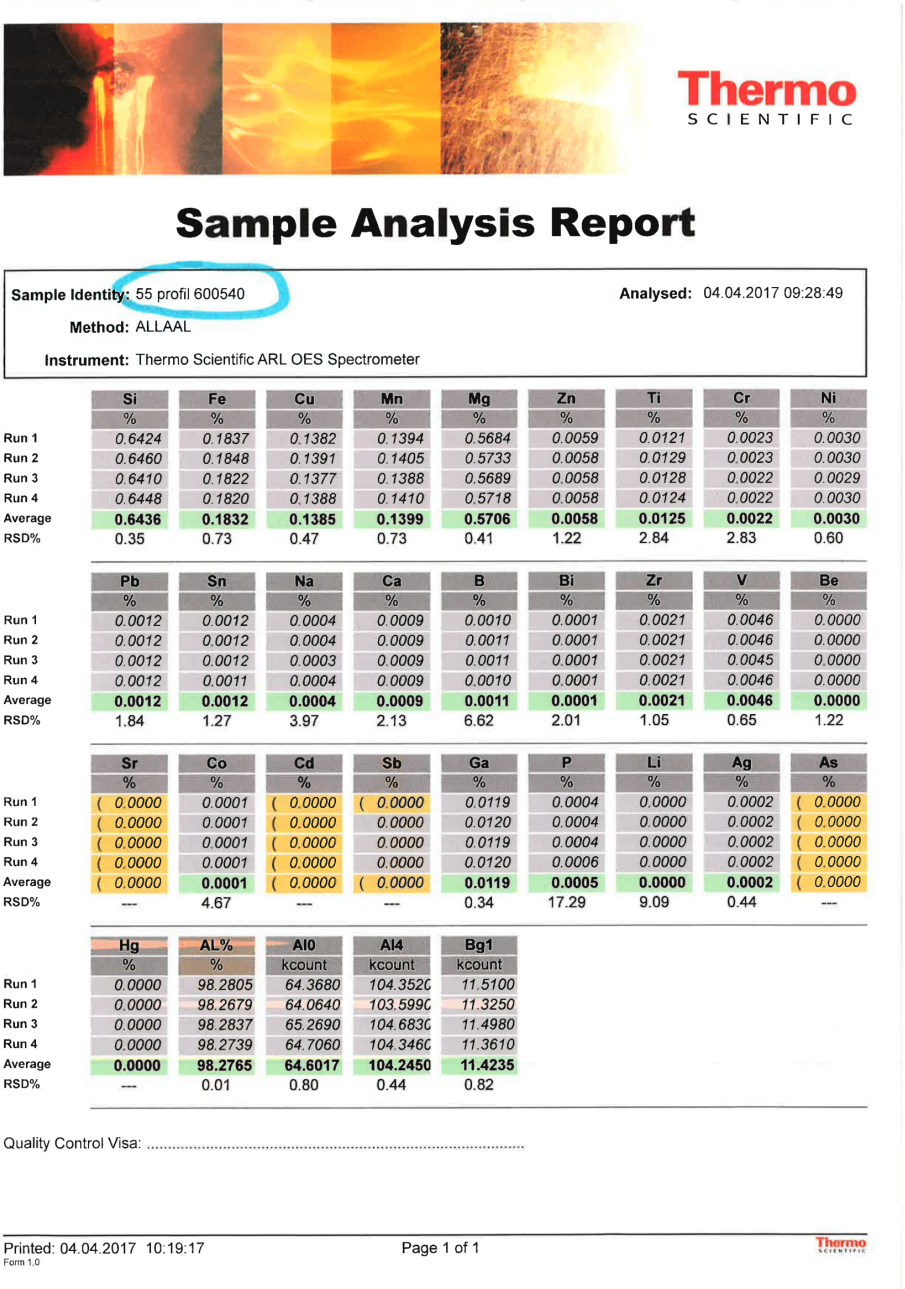

Thermo SCIENTIFIC

Sample Analysis Report

Sample Identity: 55 profil 600540 **Analysed:** 04.04.2017 09:28:49

Method: ALLAAL

Instrument: Thermo Scientific ARL OES Spectrometer

	Si	Fe	Cu	Mn	Mg	Zn	Ti	Cr	Ni
	%	%	%	%	%	%	%	%	%
Run 1	0.6424	0.1837	0.1382	0.1394	0.5684	0.0059	0.0121	0.0023	0.0030
Run 2	0.6460	0.1848	0.1391	0.1405	0.5733	0.0058	0.0129	0.0023	0.0030
Run 3	0.6410	0.1822	0.1377	0.1388	0.5689	0.0058	0.0128	0.0022	0.0029
Run 4	0.6448	0.1820	0.1388	0.1410	0.5718	0.0058	0.0124	0.0022	0.0030
Average	**0.6436**	**0.1832**	**0.1385**	**0.1399**	**0.5706**	**0.0058**	**0.0125**	**0.0022**	**0.0030**
RSD%	0.35	0.73	0.47	0.73	0.41	1.22	2.84	2.83	0.60

	Pb	Sn	Na	Ca	B	Bi	Zr	V	Be
	%	%	%	%	%	%	%	%	%
Run 1	0.0012	0.0012	0.0004	0.0009	0.0010	0.0001	0.0021	0.0046	0.0000
Run 2	0.0012	0.0012	0.0004	0.0009	0.0011	0.0001	0.0021	0.0046	0.0000
Run 3	0.0012	0.0012	0.0003	0.0009	0.0011	0.0001	0.0021	0.0045	0.0000
Run 4	0.0012	0.0011	0.0004	0.0009	0.0010	0.0001	0.0021	0.0046	0.0000
Average	**0.0012**	**0.0012**	**0.0004**	**0.0009**	**0.0011**	**0.0001**	**0.0021**	**0.0046**	**0.0000**
RSD%	1.84	1.27	3.97	2.13	6.62	2.01	1.05	0.65	1.22

	Sr	Co	Cd	Sb	Ga	P	Li	Ag	As
	%	%	%	%	%	%	%	%	%
Run 1	(0.0000	0.0001	(0.0000	(0.0000	0.0119	0.0004	0.0000	0.0002	(0.0000
Run 2	(0.0000	0.0001	(0.0000	0.0000	0.0120	0.0004	0.0000	0.0002	(0.0000
Run 3	(0.0000	0.0001	(0.0000	0.0000	0.0119	0.0004	0.0000	0.0002	(0.0000
Run 4	(0.0000	0.0001	(0.0000	0.0000	0.0120	0.0006	0.0000	0.0002	(0.0000
Average	(0.0000	**0.0001**	(0.0000	(0.0000	**0.0119**	**0.0005**	**0.0000**	**0.0002**	(0.0000
RSD%	---	4.67	---	---	0.34	17.29	9.09	0.44	---

	Hg	AL%	Al0	Al4	Bg1
	%	%	kcount	kcount	kcount
Run 1	0.0000	98.2805	64.3680	104.352(	11.5100
Run 2	0.0000	98.2679	64.0640	103.599(	11.3250
Run 3	0.0000	98.2837	65.2690	104.683(	11.4980
Run 4	0.0000	98.2739	64.7060	104.346(	11.3610
Average	**0.0000**	**98.2765**	**64.6017**	**104.2450**	**11.4235**
RSD%	---	0.01	0.80	0.44	0.82

Quality Control Visa: .....

Printed: 04.04.2017 10:19:17 Page 1 of 1 Thermo SCIENTIFIC

Form 1.0

Appendix D

Extrusion parameters and Force vs. Extrusion Speed Plot of AA6005

Material		Parameters							
	V_{ram} (mm/s)		T_{billet} (°C)			$T_{control}$ (°C)	T_{ram} (°C)	Force (kN)	
	Setpoint	Actual	Setpoint	Front	Rear			Max	Min
AA6005	5	5.1	480	489	479	425	116	3007	2292

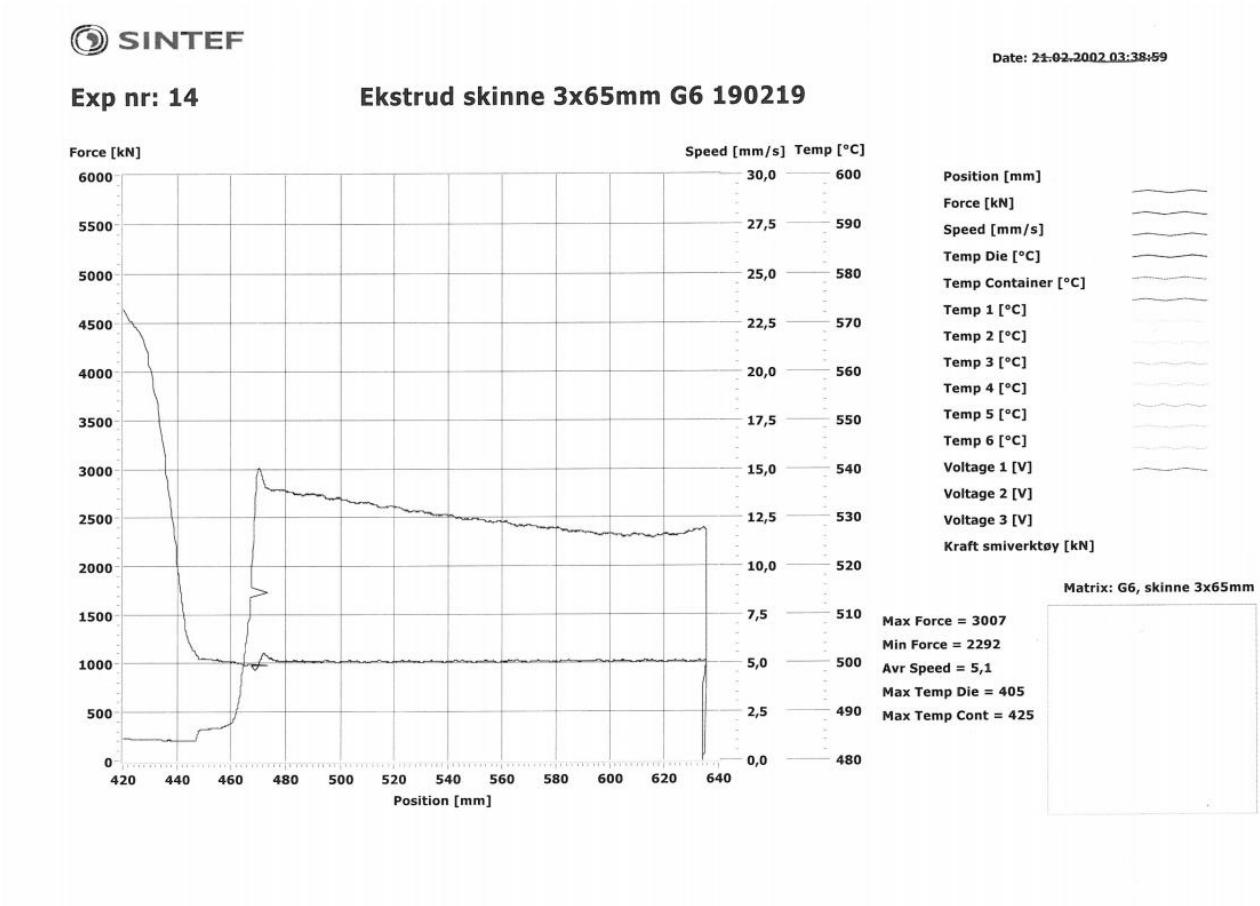

Appendix E

Hardness Measurements

Hardness measurements given in HV1 (1 kg load). WQ and AC indicated respectively water quenched and air-cooled AA6005.

Measurement number	1	2	3	4	5	6	7	8	Average	Standard deviation
WQ T4	48	48	47	47	43	49	55	58	49.4	4.81
WQ T6x	76	71	72	67	69	66	63	65	68.6	4.24
WQ T6	83	89	90	84	86	83	86	87	86.0	2.62
WQ T7	83	78	81	87	82	78	74	79	80.3	3.92
AC T4	57	54	48	55	55	47	55	58	53.6	4.00
AC T6x	60	59	61	59	60	57	57	59	59.0	1.41
AC T6	83	86	81	79	79	76	82	86	81.5	3.51
AC T7	79	87	83	80	86	85	78	85	82.9	3.44
Reference T6	98	98	97	95	97	99	99	96	97.4	1.41
Reference T7	95	88	95	93	91	91	92	92	92.1	2.30

Appendix F

Conductivity Measurements

Measured electrical conductivity given in MS/m. WQ and AC indicated respectively water quenched and air-cooled AA6005.

Measurement number	1	2	3	4	5	6	7	8	Average	Standard deviation
WQ T4	29.05	28.96	29.08	29.11	29.15	28.87	28.98	28.99	29.0	0.09
WQ T6x	29.99	29.93	29.94	30.00	29.82	29.84	29.84	29.80	29.9	0.08
WQ T6	32.21	32.18	32.13	32.14	32.27	32.09	32.18	32.19	32.2	0.05
WQ T7	32.43	32.42	32.51	32.41	32.43	32.53	32.55	32.54	32.5	0.06
AC T4	29.24	29.02	29.00	29.02	29.02	29.14	29.19	29.13	29.1	0.09
AC T6x	29.99	29.96	29.87	29.87	30.01	29.89	29.99	29.98	29.9	0.06
AC T6	32.30	32.30	32.34	32.23	32.33	32.28	32.32	32.24	32.3	0.04
AC T7	32.67	32.69	32.62	32.60	32.55	32.63	32.63	32.60	32.6	0.04
Reference T6	29.07	29.06	29.06	29.08	29.06	29.06	29.05	29.05	29.06	0.01
Reference T7	29.51	29.50	29.49	29.48	29.51	29.53	29.49	29.53	29.51	0.02

Appendix G

Pole Figures – AA6005 T6

Pole figures of Fe- and Mn-reduced AA6005 show different textures in the surface region and within the bulk. Bulk region exhibit cubic texture, while the surface region shows a rotated cube, reflecting the shear deformations on the surface.

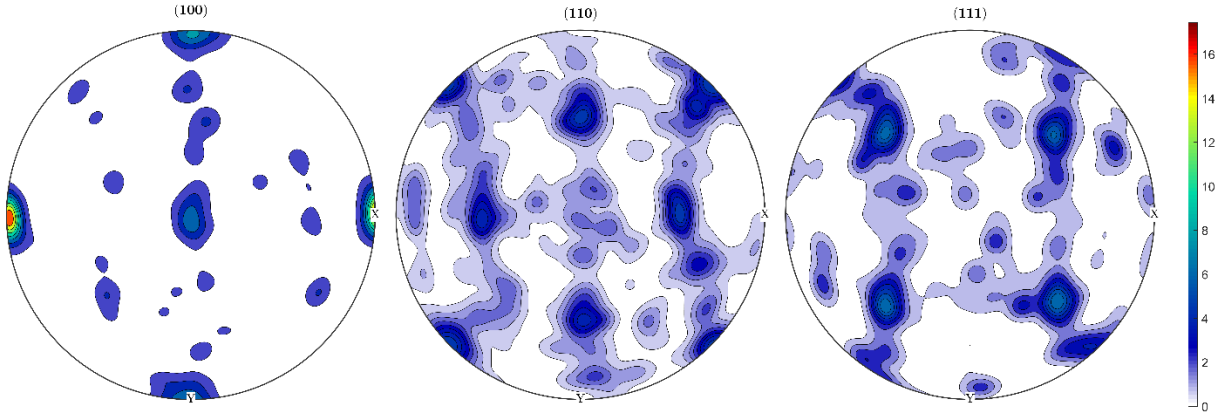

a) *Pole figure of the surface region including scale bar.*

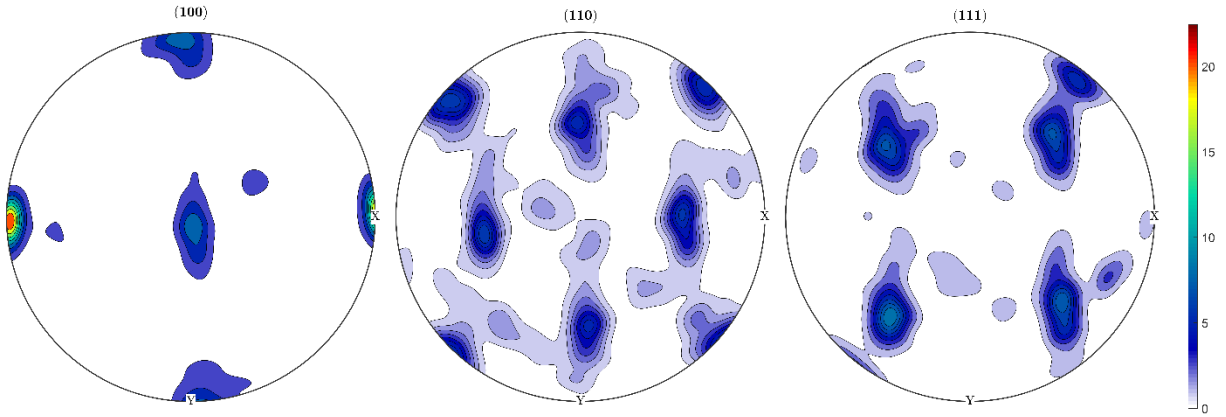

b) *Pole figure of the bulk region including scale bar.*

Pole Figures – AA600540 reference T6

Pole figures of the AA600540 reference alloy show different textures in the surface region and within the bulk. Bulk region exhibit cubic texture, while the surface region shows a rotated cube, reflecting the shear deformations on the surface.

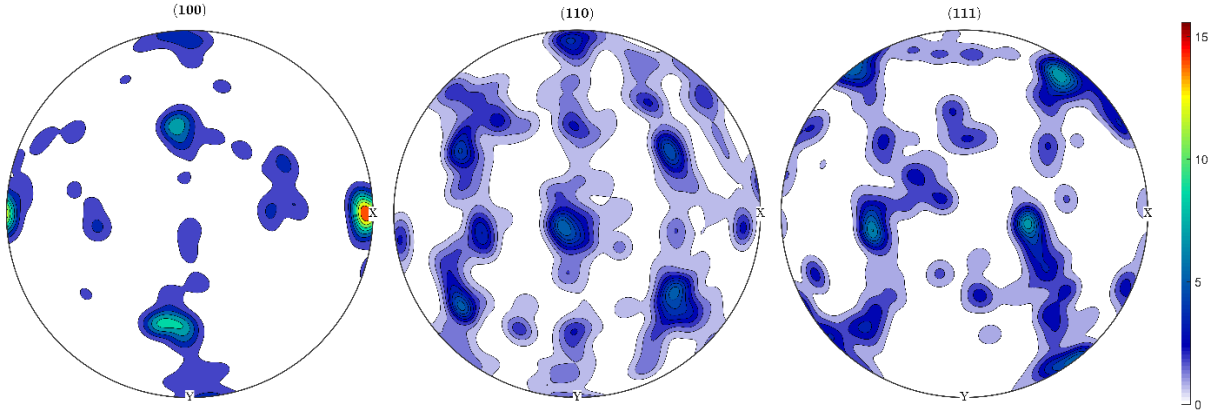

a) *Pole figure of the surface region including scale bar.*

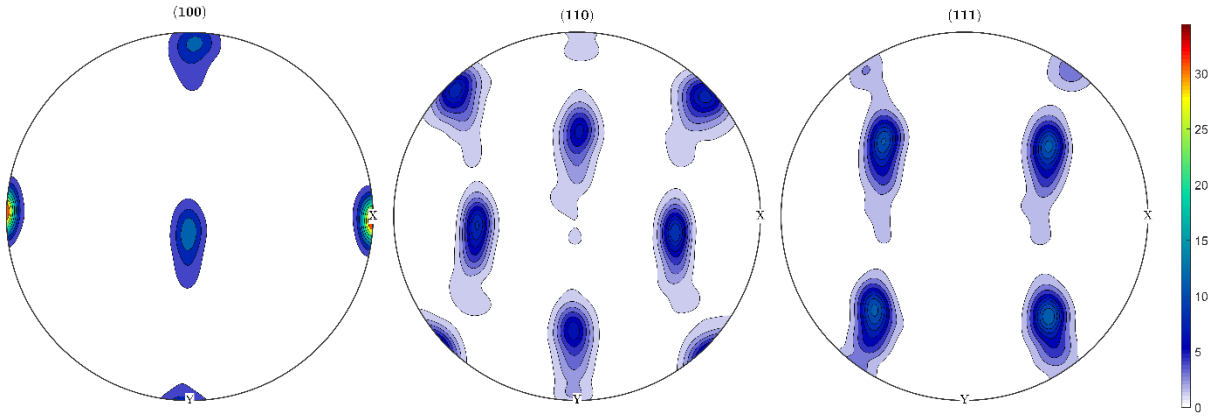

b) *Pole figure of the bulk including scale bar.*

Appendix H

Results of Accelerated Corrosion Tests

Average mass reduction per sample surface are due to accelerated IGC tests given in mg/cm^2.

Exposure time [h]	AA6005 T4	AA6005 T6x	AA6005 T6	AA6005 T7	AA6005.40 T6	AA6005.40 T7
1	0.00	0.01	0.01	0.00	0.02	0.03
5	0.12	0.12	0.11	0.08	0.58	0.58
10	0.24	0.38	0.28	0.30	2.11	1.92
20	0.40	0.54	0.51	0.52	4.85	6.61
24	0.48	0.64	0.69	0.70	5.53	6.23
48	1.32	2.22	1.43	1.23	14.81	21.95
72	1.66	3.82	2.31	1.85	18.29	26.70
96	2.33	4.73	2.08	1.85	19.67	29.02
120	2.65	4.68	2.21	2.34	23.29	32.58

Maximum penetration depth vs. exposure time to accelerated IGC tests given in µm.

Exposure time [h]	AA6005 T4	AA6005 T6x	AA6005 T6	AA6005 T7	AA6005.40 T6	AA6005.40 T7
1	0	0	0	0	53.8	126.7
5	0	0	0	0	246.7	190.8
10	36.4	129.7	0	0	280	318.5
20	0	101.5	346.7	0	409.7	249.2
24	47.2	0	356.4	0	445.6	366.7
48	184.1	230.8	344.1	417.4	497.9	481
72	43.1	214	317.4	307.2	499.9	514.9
96	17.9	292.3	467.2	419.5	526.1	543.6
120	68.2	263.1	372.1	367.7	437.9	483.1